Characterization
and Microstructural Evolution Model
of a Nb Ferrite-Bainite Steel

by

Sepehr Gerami

A THESIS SUBMITTED IN PARTIAL FULFILLMENT

OF THE REQUIREMENTS FOR THE DEGREE OF

MASTER OF APPLIED SCIENCE

in

THE FACULTY OF GRAUDATE STUDIES

(Materials Engineering)

THE UNIVERSITY OF BRITISH COLUMBIA

(Vancouver)

September 2010

Abstract

Complete microstructural evolution models for dual phase ferrite-bainite micro-alloy steels do not yet exist despite their widespread use. An attempt is made here to make a contribution towards development of a unified model. Transformation behaviour in a niobium bearing line-pipe steel is investigated. Grain growth and recrystallization studies are performed, and the results used to design continuous cooling transformation tests to study the effects of prior austenite grain size, cooling rate, retained strain, and niobium dissolution on transformation behaviour in the steel. Existing modelling techniques are then applied to the experimental data in order to predict ferrite and bainite transformation start temperatures and transformation kinetics.

Table of Contents

List of Tables

List of Figures

Acknowledgements

I would like to express my gratitude to my supervisor, Professor Matthias Militzer, for his continuous guidance and encouragement, without which this work would have certainly not been possible.

My thanks to Dr. Fateh Fazeli for his infinite patience, and invaluable assistance. I am also grateful to Dr. Sujay Sarkar and Mr. Hamid Azizi-Alizamini for their advice and our fruitful discussions.

I would like to thank Dr. Dongsheng Liu, Ms. Mary Fletcher, Mr. Ross McLeod, Mr. Carl Ng, and Mr. David Torok for their assistance in sample preparation and experimental work.

Finally, I must state that I am eternally indebted to my beloved parents for their unwavering support throughout my studies, both material and otherwise.

Chapter 1

Introduction

Steel remains as the most ubiquitous class of alloys in use today, with a wide variety of applications ranging from building structures to auto-bodies. Lowering energy consumption (and thus carbon emissions) and reducing manufacturing costs provide incentives for continued investment in research and development of modern steels. Increasing commercial interest in high strength steels in the 1970's led to the development of High Strength Low Alloy (HSLA) steels, which are commonly created by micro-alloying low carbon steels with one or more elements such as niobium, titanium, or vanadium.

In these steels, it is possible to achieve a significant improvement in yield strength through the combined effect of a refinement in grain size and dispersion hardening by second phase precipitates in a typical microstructure of ferrite and pearlite by careful control of the hot rolling process (ie: temperature and strain) [1, 2]. The development of mathematical models meant to improve process control was begun in the 1980's starting with works such as that of Sellars et al. [3] to describe the effect of hot rolling process variables, namely heating and cooling rates and strain and strain rates, on grain growth, recovery and recrystallization, and phase transformations in the steel. Complete computer process models were developed for the hot rolling of low carbon and HSLA steels [4, 5, 6].

CHAPTER 1. INTRODUCTION

More modern developments in steels have led to introduction of advanced high strength steels (AHSS), including dual phase (DP), transformation induced plasticity (TRIP) and complex phase (CP) steels. Applications for these steels range from automobile structures to oil and gas pipelines. The development of process models for these steels is still in its infancy [7], however, some preliminary models have been proposed for ferrte/martensite DP steels [8, 9], TRIP steels [10, 11], and CP steels [12].

The strength and formability of the final product can be tailored to the application by adjusting processing parameters in order to modify the proportions of each microstructural constituent. A microstructure model that would describe the decomposition of austenite according to the process parameters is therefore highly desirable. The complexity of transformation behaviour in these alloys makes developing a process model quite challenging.

The present investigation is concerned primarily on the effect of thermo-mechanical processing parameters on the phase transformation behaviour of a niobium bearing ferrite/bainite steel with a more complex-type microstructure. There is a need for the development of models for ferrite-bainite steels, and so an attempt is made to utilize existing modelling techniques to reproduce experimental data.

Chapter 2

Objectives

The main objectives of this study are to:

- Characterize the transformation behaviour of the complex phase steel - Investigate the effect of cooling rate, initial austenite grain size, and retained strain on austenite decomposition temperature, transformation kinetics, and final microstructure.

- Quantify the effect of the state of niobium dissolution on the transformation behaviour of the steel.

- Utilize existing modelling techniques to develop a model that can predict the transformation kinetics and final microstructure of the steel.

Chapter 3

Literature Review

As face centred cubic (FCC) austenite (γ) is cooled beyond the A_3 or A_cm lines on the iron-carbon binary phase diagram (figure 3.1), it begins to transform to a body centred cubic (BCC) crystal structure referred to as 'ferrite' [13]. In a binary iron-carbon system at equilibrium, the steel is entirely BCC below $\sim$ 725°C. Depending on the concentration of carbon and processing parameters, a certain amount of iron carbide (Fe_3C) termed 'cementite' can precipitate upon cooling during and/or after transformation below the A_1 and A_cm lines in the phase diagram. At lower temperatures, metastable body centred tetragonal (BCT) martensite forms. Microstructural constituents consisting of these components are classified as grain boundary ferrite, grain boundary cementite, massive ferrite, Widmanstätten ferrite, Widmanstätten cementite, pearlite, upper bainite, lower bainite, lath martensite, and twinned martensite [14]. In the present study, grain boundary cementite, Widmanstätten cementite and massive ferrite are not encountered.

At small undercoolings below A_3, ferrite (α) nucleates on austenite grain boundaries and grows in a 'blocky' manner into approximately equiaxed grains[16]. Ferrite nucleating and growing on austenite grain boundaries under moderate undercoolings is referred to as grain boundary or 'allotriomorphic' ferrite. Below the A_1 line in the phase diagram (reported as 0.76wt%

Figure 3.1: The iron-carbon binary phase diagram [15]

in figure 3.1) where untransformed austenite is supersaturated with carbon - due the bulk concentration of the steel or carbon rejection from ferrite to austenite during ferrite formation - a eutectoid product called 'pearlite' forms [16].

At higher cooling rates ferrite assumes non-polygonal acicular morphologies. With a further increase in cooling rate, austenite decomposes into a needle or plate like ferritic structure that grows from existing ferrite allotriomorphs, referred to as 'Widmanstätten ferrite'. At lower temperature under these higher cooling rates, a eutectoid product structurally distinct from pearlite, termed 'bainite', can form. The exact morphology of bainite is heavily dependent on its temperature of formation [16]; it is often categorized as either upper or lower bainite. The general morphology is that of aggregates of ferritic platelets separated by regions of residual phases, usually consisting of untransformed austenite, martensite and/or cementite. These

aggregates are referred to as "sheaves" [17]. Widmanstätten ferrite is structurally similar to the ferritic portion of bainite, such that it can be difficult to distinguish the two under an optical microscope.

Both semi-empirical and theoretical models have been developed in an attempt to predict phase transformation behaviour in steels. The following sections discuss some of these approaches.

3.1 Semi-Empirical Models

Models for phase transformations in low carbon steels typically consist of distinct steps: Prediction of the ferrite transformation start, ferrite transformation kinetics, pearlite and/or bainite transformation start, and pearlite and/or bainite transformation kinetics.

3.1.1 Ferrite Formation Start

The ferrite transformation start temperature is often calculated thermodynamically; assuming equilibrium, the point at which ferrite formation starts is where the alloy temperature drops below the Ae_3 line on the iron-carbon phase diagram [4, 5]. This approach does not take the condition of the austenite into consideration, however.

Militzer et al. [18] suggested a method of predicting early growth of corner nucleated ferrite based on the austenite grain size and cooling rate. The approach assumes that nucleation site saturation is in effect beyond 5% of austenite decomposed, and that carbon diffusion is rate controlling. Under local equilibrium conditions, the temperature at which 5% of austenite has decomposed is taken as the experimentally detectable transformation start temperature T_S, which is evaluated from:
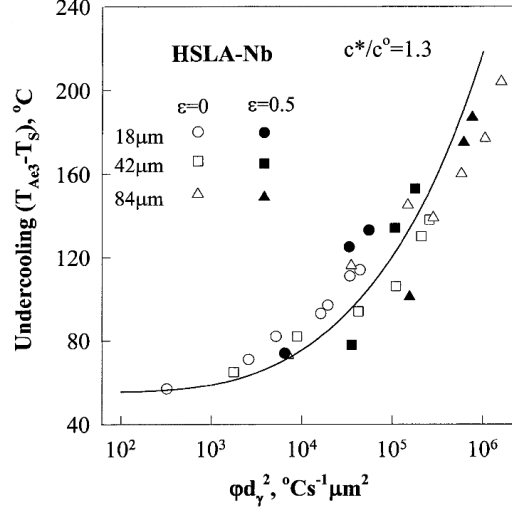
Figure 3.2: An example of the ferrite start model of Militzer et al. [19]

$$X_C^* - X_C^\circ = \frac{\sqrt{2M_P}\,(X_C^* - X_C^\circ)}{\phi^{1/2}d_\gamma}\sqrt{\int_{T_S}^{T_N} D_C \frac{X_C^I - X_C^\circ}{X_C^I - X_C^\alpha}\,dT} \qquad (3.1)$$

where X_C° is the bulk concentration of carbon in the steel, X_C^* is the limiting local carbon concentration at nucleation site saturation, $M_P \sim 2$ is the number of ferrite nuclei per austenite grain, ϕ is the cooling rate, d_γ is the austenite grain diameter, T_N is the temperature of nucleation, D_C is the diffusivity coefficient of carbon in austenite, X_C^I is the concentration of carbon at the ferrite/austenite interface, and X_C^α is the concentration of carbon in ferrite. X_C^* and T_N are used as fit parameters. An example of the model is shown in is shown in figure 3.2. The points show experimental data, while the solid line represents the model.

3.1.2 Transformation Kinetics

The Johnson-Mehl-Avrami-Kolmogorov (JMAK) equation [20, 21, 22, 23, 24] is often used to describe isothermal phase transformation kinetics. It provides a less numerically intensive semi-empirical method of predicting transformation rates based on experimental data, without requiring diffusivity and mobility data. In general form, the JMAK equation is written as:

$$X^\alpha = 1 - \exp\left(-bt^n\right) \tag{3.2}$$

The constants b and n are often empirically determined, and are reflective of growth and nucleation conditions. The JMAK equation has been widely used to describe the formation of ferrite, pearlite, and bainite. Where more than one of these constituents is present, the JMAK equation is applied separately to each of them using different sets of parameters. Various modifications of the equation have been used. Table 3.1 lists some of the forms of the equation and their associated parameters available in literature. Commonly, the rate parameter b is defined as a function of chemical composition, temperature, carbon supersaturation, prior austenite grain size, strain, and/or cooling rate.

In their application of the JMAK equation to ferrite transformation, Liu et al. [7] and Militzer et al. [19] normalized the fraction of ferrite formed to the equilibrium ferrite fraction X^e. They utilized a modified form of the JMAK equation proposed by Umemoto et al. [25]:

$$X = 1 - \exp\left(\frac{-bt^n}{D_\gamma^m}\right) \tag{3.3}$$

Nominal values for the parameters n and m in equation 3.3 are shown in table 3.2. Sarkar et al. chose to integrate the effect of D_γ into the parameter b. In the work of Han and Park [26] the values of b and n are functions of the

steel chemical composition. In contrast, the other authors chose a constant n independent of composition.

Application of the Additivity Rule to the JMAK Equation

Both nucleation and growth rates are temperature dependent. Consequently, they will be time dependent if the temperature of transformation varies with time. This makes application of the JMAK equation to continuous cooling transformations problematic. To counter this problem, Avrami [21] defined an "isokinetic" range of temperatures and concentrations in a given substance where the kinetics of phase change in the characteristic time scale remains unchanged; the relative internal history of the transformation is independent of the temperature path provided nucleation rate $\dot{N}$ and growth rate $\dot{I}$ are proportional. Within this specific range, isothermal data can be used in conjunction with the principle of additivity [28] to describe the reaction under non-isothermal conditions. The principal requirement for additivity is:

$$\int \frac{\mathrm{d}t}{\tau} = 1 \tag{3.4}$$

That is, in a certain reaction where isothermal time τ results in a fraction transformed $X_\circ$, the reaction would reach $X_\circ$ under continuous cooling at a time t and temperature T where the above integral becomes unity.

Cahn [29] suggested any reaction would be additive provided that the rate of transformation $\mathrm{d}X/\mathrm{d}t$ was an exclusive function of temperature and the amount of parent material transformed:

$$\frac{\mathrm{d}X}{\mathrm{d}t} = \left[\frac{\mathrm{d}H(X)}{\mathrm{d}X} \right]^{-1} h(T) \tag{3.5}$$

Table 3.1: Variations of JMAK equation and associated parameters in previous studies

Alloy Composition (wt%)	Transformation	JMAK Equation and Parameters
Han and Park [26] Fe-0.2C-1.97Si-1.52Mn-0.05Al-0.05Nb	Ferrite	$X = 1 - \exp\left(-bt^n\right)$ $\ln b = 2.58445 + 1.845\ln(AGS)(4.5407 + 167.707[\%C_\gamma] - 67201[\%C_\gamma]^{1/2}) \times$ $\ln(T_{Ae3} - T) + (-35684 - 877455[\%C_\gamma] + 374207[\%C_\gamma]^{1/2}/T$ $n = 0.8674 + 1.7506[\%C_\gamma] + 0.0583[\%Mn]$
Militzer et al.[19] Fe-0.04C-0.30Mn-0.040Al Fe-0.045C-0.45Mn-0.08V-0.069Si-0.078Al Fe-0.08C-0.48Mn-0.036Nb-0.045Si-0.024Al Fe-0.07C-0.76Mn-0.023Nb-0.013Ti-0.014Si-0.053Al Fe-0.07C-1.35Mn-0.086Nb-0.047Ti-0.14Si-0.044Al	Ferrite	$\frac{X}{X^e} = \left[1 - \exp\left(\frac{1}{D_\gamma^m}(\xi)^n\right)\right]$ $X^e = \frac{X_\gamma^C - X_\circ^C}{X_\gamma^C - X_\alpha^C}, \ n = 0.9$ $\xi = \int_{T_S}^{T} \frac{\exp[(b_1(T_{Ae3} - T') - b_2)/n]}{q(T')}$
Liu et al.[7] Fe-0.07C-1.45Mn-0.73Si-0.05Al-0.01Ti Fe-0.06C-1.86Mn-0.077Si-0.043Al-0.011Ti-0.155Mo	Ferrite	$\frac{X}{X^e} = \left[1 - \exp\left(-b\frac{t^n}{D_\gamma^m}\right)\right]$ $X^e = \frac{X_\gamma^C - X_\circ^C}{X_\gamma^C - X_\alpha^C}, \ n = 1$ $b = \exp B_\circ + B_1(T_{Ae3} - T) + B_2\frac{X_\circ^C}{1-X}$
Sarkar et al.[12] Fe-0.05C-1.88Mn-0.04Si-0.048Nb-0.49Mo-0.05Al	Ferrite	$X = 1 - \exp\left(-bt^n\right)$ $\ln b = A_0 + A_1T + A_2\ln D_\gamma, \ n = 1.1$
	Bainite	$\ln b = B_0 + B_1T + B_2\left(X_\gamma^C \ln\left(D_{\gamma,rem}\right)\right), \ n = 0.85,$ $D_{\gamma,rem} = $ untransformed γ grain diameter

Table 3.2: Nominal JMAK parameters for Umemoto Model [27]

Nucleation Site	Site Saturation		Nucleation & Growth	
	n	m	n	m
Grain Surface	1	1	4	4
Grain Edge	2	2	4	2
Grain Corner	3	3	4	3

Avrami's requirement that $\dot{I} \propto \dot{G}$ is rarely fulfilled in real reactions. However, in many cases of heterogeneous nucleation, the rate of nucleation is high, and potential nucleation sites are quickly exhausted as a consequence [30]. The reaction then becomes a function of growth rate only, which satisfies conditions for additivity.

The JMAK equation in conjunction with the additivity principle is often used [7, 10, 12, 31, 32] as a convenient semi-empirical method to model the continuous cooling behaviour of austenite decomposition. In such a model, the reaction is broken down into isothermal increments, and the rate of transformation is calculated at each increment. The fraction transformed during each time increment is then simply the rate of transformation in that time increment multiplied by the length of the time increment.

The b and n parameters in the JMAK equation are often optimized through mathematical means [33, 12]. Rios [34] devised a method of extracting b and n from continuous cooling data which is based on a theoretical rather than the usual mathematical approach. Some limitations to this model have been identified by Jia and Militzer [35], and some modifications have been made by the authors to address these limitations [35]. Descriptions of Rios' approach, and said modifications, are provided in chapter 6.

3.1.3 Ferrite Stop/Bainite Start

The transition point between ferrite and pearlite and/or bainite transformation is modelled by some authors [5, 4] by employing empirical relationships derived from experimental data in specific steels. There has been an effort by others [12, 10, 36], to utilize a more meaningful approach. The transition from ferrite to bainite is analyzed by these authors using the driving force for bainitic ferrite formation, as suggested by Ali and Bhadeshia [37]. Ali and Bhadeshia found that the free energy needed to obtain a detectable degree of bainitic ferrite formation could be approximated as a linear function of temperature, applicable to any low alloy steel.

Bainite formation is assumed to take place under para-equilibrium conditions (carbon atoms may diffuse to reach a state of equilibrium but no diffusion of substitutional solutes takes place). Using thermodynamic data for the steel studied, the driving pressure ΔG for the formation of the bainitic ferrite can be calculated at any point during austenite decomposition, using the instantaneous temperature and carbon content in the remaining austenite. The critical driving pressure ΔG_{bs}^* at which bainite formation starts is defined as the free energy calculated at an experimentally derived bainite transformation start temperature and corresponding austenite carbon concentration. Plotting the critical driving pressure vs bainite start temperature, Sarkar, Liu, Fazeli and co-workers [12, 10, 36] found that a linear relationship existed between the two, regardless of carbon content and austenite microstructure, similar to the function found by Ali and Bhadeshia. These linear relationships can be seen in figure 3.3. Fazeli et al.[36] explained the discrepancy between their results and that of Ali and Bhadeshia [37] as a consequence of using different thermodynamic models and databases.
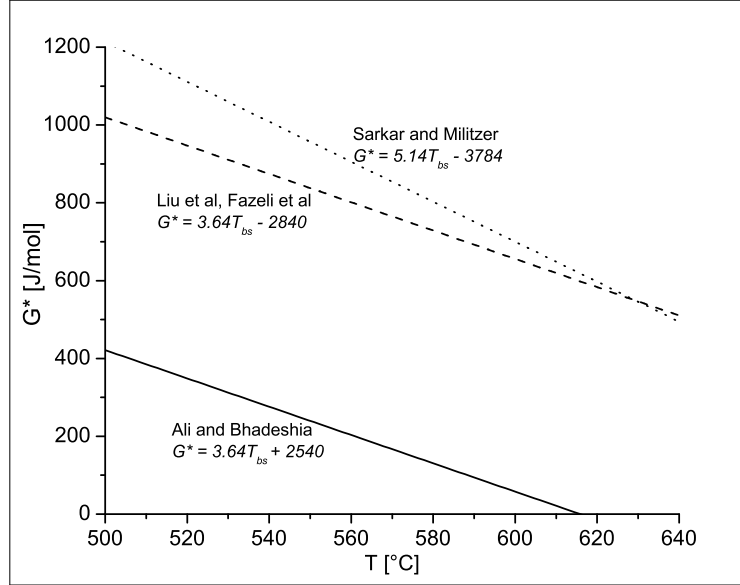
Figure 3.3: Critical driving pressure G^* vs bainite start temperature T_{bs} from studies by Liu et al.[10], Fazeli et al.[36], Sarkar and Militzer [12] and Ali and Bhadeshia [37]

3.2 Theoretical Approaches

3.2.1 Ferrite Formation

Nucleation

The net free energy change during ferrite nucleation consists of several contributions: The volume free energy reduction $V\Delta G_V$ associated with formation of BCC crystal, the free energy increase $A\sigma$ due to the creation of an area A of FCC-BCC interface, the volume free energy change $V\Delta G_S$ associated with the misfit strain caused by the difference between the lattice parameter of the FCC and BCC crystals, and the free energy drop ΔG_d associated with

the destruction of austenite grain boundary[16]:

$$\Delta G^* = -V\Delta G_V + \sum A_i\sigma_i + V\Delta G_S + \Delta G_d \tag{3.6}$$

The sum in the interfacial energy term in equation 3.6 reflects the fact that ferrite nuclei do not form with isotropic interfaces, but rather do so surrounded by interfaces of varying energy. By classical nucleation theory, the time-dependent nucleation rate is given by [38]:

$$\dot{I} = N\beta Z \exp\left(-\frac{\Delta G^*}{kT}\right)\exp\left(-\frac{\tau}{t}\right) \tag{3.7}$$

where N is the density of viable nucleation sites, β^* is the frequency factor, Z is the Zeldovich non-equilibrium factor, τ is the incubation time, t is the isothermal reaction time, k is the Boltzmann constant, and T is temperature. Nucleation is considered to occur first on grain corners, followed by grain edges, and finally, grain faces.

Before ΔG^* can be calculated, information about the critical nucleus interface and shape is required. Assuming that the nucleus interface is isotropic would cause the interface to curve out evenly into the parent phase; as such, an incoherent ferrite nucleus on an austenite grain boundary can be assumed to be in the shape of two spherical caps. Clemm and Fisher [39] arrived at the following relation for ΔG^*:

$$\Delta G^* = \frac{4\left(z_2\sigma_{\alpha\gamma} - z_1\sigma_{\gamma\gamma}\right)^3}{27z_3\Delta G_V^2} \tag{3.8}$$

where $\sigma_{\alpha\gamma}$ and $\sigma_{\gamma\gamma}$ are the interfacial energies for the ferrite/austenite interface and austenite grain boundaries, respectively. The parameters z_1 through

14

z_3 are factors dependent on the geometry of the nucleus and the ratio $\sigma_{\alpha\gamma}/\sigma_{\gamma\gamma}$. The misfit strain energy ΔG_S is neglected. Although the spherical cap model is commonly used in classical analytical nucleation rate calculations, it fails to predict experimental data [40].

Lange, Enomoto and Aaronson [38, 41, 42, 40] developed a revision of the classical approach by using several different "pill-box" shaped nuclei of different geometries: either with a very low energy edge and two low energy planar faces, or with a low energy edge, a planar low energy face and a spherical cap high energy face. The authors reported good agreement of their model with experimental data for Fe-C and Fe-C-X alloys (where X represents some substitutional alloying element), provided nucleation was permitted at a very small fraction of the atomic sites available at grain faces. It must be noted, however, that in their observation of nucleation and growth kinetics of ferrite using X-ray diffraction patterns at a synchrotron facility, Offerman et al.[43] found that the activation energy for nucleation calculated by the method of Lange et al.[40] was two orders of magnitude larger than what they observed experimentally.

Growth

The hypoeutectoid portion of the iron-carbon phase diagram can be seen Figure 3.4 [32]. As a plain carbon steel with a carbon concentration of $C_{\circ}$ is cooled below the Ae_3 line to $T = T_1$ under equilibrium conditions, ferrite begins to precipitate and grow with a concentration given by the $\gamma/\gamma + \alpha$ phase boundary line at T_1, $C_{\alpha 1}$. Carbon rejected from the ferrite diffuses into the parent austenite, such that the concentration of carbon in austenite immediately adjacent to the growing ferrite grain is given by the Ae_3 (or $\gamma + \alpha/\gamma$ boundary) line at that temperature, $C_{\gamma 1}$. Further cooling to T_2 results in a carbon concentration of $C_{\alpha 2}$ in the ferrite, and $C_{\gamma 2}$ in the austenite at the interphase. Under this mechanism, the transformation is said to be diffusion controlled.
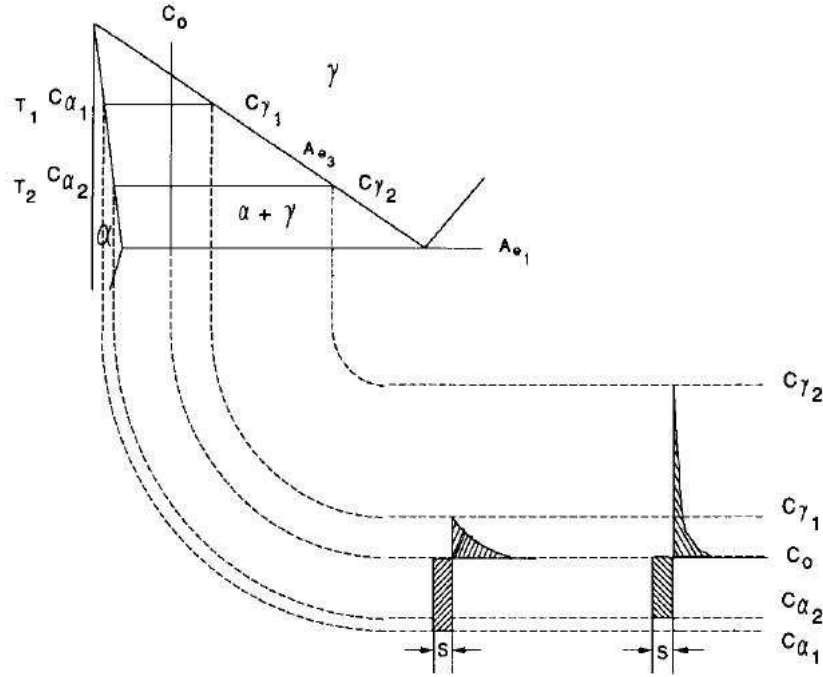
Figure 3.4: Iron-carbon phase diagram and concentration profiles [32].

The lower part of figure 3.4 represents the carbon concentration profiles in the ferrite and austenite. It can be seen that the carbon concentration in austenite drops as one moves away from the growing ferrite grain. The shape of the carbon profile in the austenite is due to the diffusion of carbon atoms away from the enriched boundary and into the bulk of the parent austenite. The diffusion of carbon in austenite determines the degree of pile-up of carbon atoms at the interphase. Under these conditions, diffusivity in the austenite is therefore the rate limiting parameter in the formation of ferrite.

During the initial stages of growth the bulk concentration of the austenite away from the interface C_o does not increase by a significant amount, and is often considered constant. This simplification is problematic at later stages in the transformation, however, as will be discussed later.

One dimensional diffusion across the interphase is described by:

$$\frac{\partial C}{\partial t} = \frac{\partial}{\partial x} \left(D_C^\gamma \frac{\partial C}{\partial x} \right) \tag{3.9}$$

where C is the concentration of carbon in austenite, t is time, x is the distance away from the interphase into the austenite, and D_C^γ is the diffusivity of carbon in austenite. For a spherical particle with radius r:

$$\frac{\delta C}{\delta t} = \frac{\delta}{\delta r} \left(D_C^\gamma \frac{\delta C}{\delta r} \right) + \frac{2D_C^\gamma}{r} \frac{\delta C}{\delta r} \tag{3.10}$$

In reality, the transformation of austenite to ferrite involves two mechanisms: the diffusion of carbon from the ferrite product into the austenite parent, and the rearrangement of the FCC austenite crystal lattice into the BCC ferrite crystal lattice. In the carbon diffusion controlled mechanism discussed above, the greater proportion of the energy of transformation is dissipated through diffusion of solute through the solid. Where the rearrangement of atoms at the interface becomes significant, the reaction becomes 'mixed mode'. It is also possible for the transformation to become interface controlled. [44]

Under diffusion control, growth of the critical nucleus can be simplified as an advancing planar front. Zener [45] approximated the rate at which the front advances as:

$$v = \frac{X_{C,eq}^\gamma - X_C^\circ}{\sqrt{\left(X_C^\circ - X_{C,eq}^\alpha \right) \left(X_{C,eq}^\gamma - X_{C,eq}^\alpha \right)}} \sqrt{D/t} \tag{3.11}$$
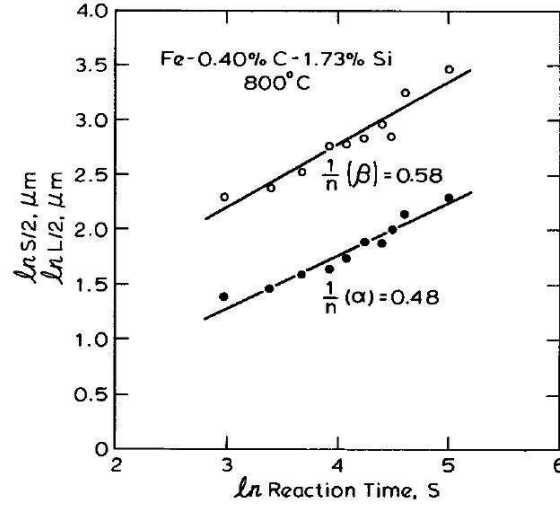
Figure 3.5: Parabolic growth of allotriomorphic ferrite. $S/2 = \alpha t^{0.5}$ and $L/2 = \beta t^{0.5}$ are the half-thickness and half-length of the allotriomorphs. α and β are the parabolic growth rate constants for thickening and lengthening [46].

where $X^{\gamma}_{C,eq}$ and $X^{\alpha}_{C,eq}$ are the equilibrium concentrations of carbon in austenite and ferrite, and X°_C is the bulk carbon concentration of the alloy.

The above simplification is not a solution of the underlying diffusion problem; however, analytical solutions of the diffusion problems confirm parabolic growth rates before soft impingement takes place [9]. This has also been verified experimentally. The data of Bradley and Aaronson [46], for instance clearly shows a parabolic relationship (figure 3.5).

The use of the carbon diffusion model to describe ferrite transformation is quite common. An example of an application is the work of Kamat et al. [32], who developed a finite difference model based on equations 3.9, 3.10 for isothermal transformation in grade 1010 and 1020 steels. Their results can be seen if figure 3.6. While the planar geometry model gives good initial agreement, later stages of the reaction are better described by the spherical geometry model.
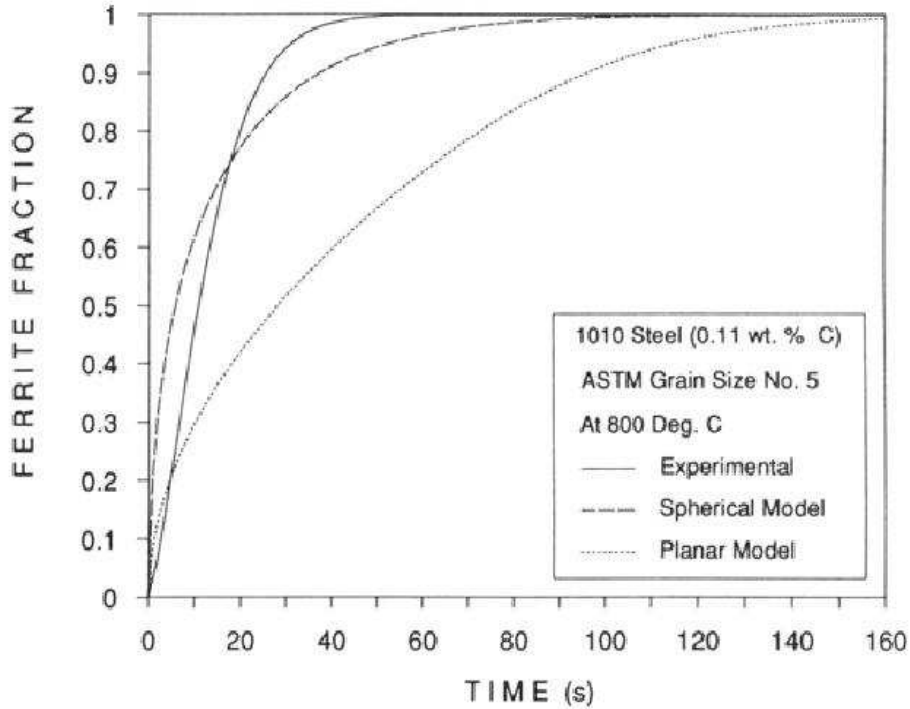
Figure 3.6: Model of Kamat et al.[32]

Investigating a ternary Fe-C-X system (where X represents a substitutional alloying element) presents complications over the simple binary Fe-C system, due to the much higher diffusivity of interstitial carbon relative to substitutional alloying elements. Since carbon diffusion is very rapid, full equilibrium can be assumed in the case of Fe-C alloys for most of the transformation. However, it is not reasonable to expect full equilibrium in substitutional alloys, since transformation rates exceed the rate of diffusion of some components in the system. Furthermore, the rate of diffusion of interstitial atoms is much higher than that of substitutional atoms. Three conditions could occur during ferrite formation: ortho-equilibrium (OE), para-equilibrium (PE) and negligible partitioning local equilibrium (NPLE) [47].

Under ortho-equilibrium, each component has equivalent chemical po-

tentials in both the parent and product phases. Both interstitial and substitutional components diffuse during transformation. Under PE, only the interstitial component (carbon) reaches a state of equilibrium; substitutional atoms are essentially immobile, such that the concentration of substitutional elements in the parent remains unchanged after transformation. Transformations under PE tend to proceed at higher rates. The third case, NPLE, is an intermediate condition between the two extremes of OE and PE; substitutional atoms can diffuse locally, but cannot reach equilibrium in the bulk phases. In systems under NPLE conditions that lie closer to PE, limited local diffusion of substitutional solutes creates a sharp spike-like pile-up of solute atoms in front of the advancing ferrite interface, yet the lack of long range diffusion leaves the bulk substitutional composition of the alloy unchanged [48, 49, 47].

In their study of ferrite growth in Fe-C-X steels, Enomoto and co-workers [38, 41, 42] carried out their calculations under OE, PE and NPLE. They found that reaction kinetics followed NPLE at higher transformation temperatures, and PE at lower transformation temperatures. A later investigation by Tanaka et al.[50, 51, 52] of transformations in quaternary Fe-C-Mn-X systems found somewhat consistent results, showing a gradual shift away from PE as transformation temperatures were increased. Rates predicted by these models typically exceed that of experimental results. This is explained by the authors as a solute drag like effect (SDLE). In this theory, the 'spike' like pileup of substitutional atoms tends to interact with the advancing phase boundary [53], reducing the interface mobility, and therefore the transformation rate.

The model of Kamat et al.[32], was applied by Militzer et al. [18] to A36 (Fe-0.17C-0.74Mn-0.012Si-0.040Al wt%) and DQSK (Fe-0.038C-0.30Mn-0.025Ni-0.033Cr-0.040Al wt%) steels transforming under continuous cooling. It was found that for the more manganese rich A36 steel, the carbon diffusion model predicted transformation rates in excess of what was experimentally observed

in the earlier stages of growth; this was attributed to the modification of carbon diffusion by solute drag due to manganese, and it was therefore necessary to reconsider the equilibrium conditions at the interphase. Considering a steady state enrichment of manganese at the interphase due to segregation, the thermodynamic conditions at the interphase were re-assessed by including a 'segregation factor' dependent on the ability of manganese to follow the movement of the interphase.

Hutchinson et al.[44] developed a carbon diffusion based model describing Fe-C-Ni alloys where they identified a transition from PE to NPLE during isothermal growth of ferrite, where the local diffusion of nickel was rate-controlling. Growth was initially fast and fit PE conditions; as growth slowed later in the reaction (presumably due to a reduction in driving force) nickel atoms had time to diffuse through the interface and a nickel spike formed in front of the interface, promoting interfacial conditions to evolve towards NPLE. The authors found good agreement with their experimental data.

3.2.2 Bainite Formation

As mentioned earlier, Widmanstätten ferrite is structurally similar to bainite. It seems to be generally accepted that Widmanstätten ferrite nucleates and grows through diffusional processes [54, 55, 49, 56]. While authors agree that the ferrite portion of bainite also nucleates through a diffusive process, there is disagreement on the growth mechanism of bainite. Two competing theories exist. The first describes bainite formation as a partially displacive mechanism where ferrite sheaves form in a manner similar to that of martensite followed by diffusion of interstitial carbon atoms into the surrounding austenite and later precipitation of cementite [55]. The second theory proposes that the ferrite in bainite (referred to hereafter as bainitic ferrite) forms by a ledge-wise diffusion mechanism, and that it is simply a microstructural continuum of pearlite [48, 57].

Displacive Theory

In displacive transformations, there is a crystallographic dependence; the habit plane of martensite is macroscopically undistorted. That is, the habit plane is common to both the austenite parent and the martensite. This is due to the displacive transformation occurring by a homogeneous shear that is parallel to the habit plane. The displacive transformation therefore induces an Invariant Plane Strain (IPS), as there are no strains in-plane. It is important to note that this requires the interphase to be glissile.

As a direct consequence of the IPS, the intersection between the surface of a specimen and of a BCC crystal growing displacively within that specimen will cause a rotation at the surface, about its intersection with the growing crystal's habit plane. This phenomenon is referred to as the surface relief effect. Reliefs on the surface of samples that have undergone bainitic transformation are cited as evidence for the displacive formation of bainite [49].

The sheaf-like morphology of the ferrite plates is attributed to deformation in the untransformed austenite as ferrite plates form; the FCC-BCC transformation is accompanied by significant dilation normal to the habit plane, which requires plastic accommodation in the adjacent austenite. Dislocations formed in the austenite cause a loss of coherency in the interphase, halting the growth process. Further growth of ferrite must then come from sympathetic nucleation of new plates, causing the sheaf-like morphology of bainite [17]. In experiments carried out by Shipway and Bhadeshia [58] bainitic ferrite formation was reduced in samples that were plastically deformed in the austenitic range, despite increased nucleation of bainite subunits due to the higher dislocation density. The authors attributed this to dislocation forests interfering with glissile requirement of the interphase.

Ferrite plates form in a displacive manner such that no diffusion of substitutional atoms, including iron atoms, takes place, and interstitial atoms diffuse only after the initial displacive reaction [59]. According to the pro-

ponents of the displacive mode of transformation, carbon diffusion is much slower than bainitic ferrite growth, as justified by direct atomic resolution image and atomic resolution chemical analysis experiments [49]. The displacively formed ferrite plates would therefore be supersaturated with carbon, which later diffuses to the austenite/ferrite interface and enriches the untransformed austenite, or precipitates as cementite. Carbon enrichment of the residual austenite can reach a level that stabilizes the austenite; the final fraction of bainite is therefore dependent on the composition of the final austenite [60].

In upper bainite, carbon is partitioned into the residual austenite, and the ferrite is largely carbide free. Cementite precipitation becomes thermodynamically possible when carbon concentration in the austenite reaches the solubility limit. Where no kinetic hindrances are present, carbide formation accompanies ferrite growth, until some limiting temperature. The precipitation of carbides from residual austenite prompts formation of secondary ferrite. Given the very low diffusivity of iron and substitutional atoms at the temperatures involved, and the supposed absence of incoherent interfaces or grain boundaries to start the process, the secondary ferrite is not likely to form through a diffusive mechanism and is far more likely to form displacively [49]. Nakamura and Nagakura [61] suggest that cementite forms directly from austenite on the ferrite-austenite interface, and grows by rapid diffusion. Ohmori and Maki [62] describe a mechanism where platelets form on the edges of the growing ferrite prior to impingement.

In lower bainite, there is a fine dispersion of plate-like carbides inside the ferrite plates, arranged along the same crystallographic direction as the ferrite plates they populate. In-situ hot-stage TEM by Kang et al.[63] showed that lower bainite ferrite remains supersaturated with carbon for some time after completion of growth. The carbides in the final product are mostly cementite, however, ϵ transition carbides have also been detected. A model, proposed by Matas and Hehemann [64] involves the formation of carbides

which then transform to cementite at a later time. There are two cases in the formation of carbides in lower bainite, that of high dislocation density, and that of low dislocation density [49].

In their model, Rees and Bhadeshia [60] consider the activation energy of bainite to be directly proportional to the driving force for bainite transformation. The nucleation mechanism of bainite is held to be identical to that of Widmanstättätten ferrite. Nucleation is therefore only possible below the Widmanstättätten ferrite start temperature W_S. A function $G_N(T)$ is defined that describes the universal value of the minimum free energy change for displacive nucleation of ferrite. Ali and Bhadeshia [37] propose a linear relationship between G_N and temperature, based on experimental data. Work by Sarkar and Militzer [12] seems to confirm this.

The model of Rees and Bhadeshia [60, 65] is as follows. The nucleation rate I is given by equation 3.12:

$$I_\circ = K_1 \exp\left[-\frac{K_2}{RT} - \frac{K_2 \Delta G_m}{rRT}\right] \tag{3.12}$$

where r, K_1 and K_2 are empirical constants. K_1 is representative of the density of potential sites for nucleation, and at W_S, $I = K_1$. ΔG_m is the maximum free energy available for para-equilibrium nucleation, calculated using a parallel tangent construction [66]. For nucleation to proceed, $\Delta G_m < G_N$.

Driving force for nucleation decreases as the transformation proceeds due to carbon enrichment of the parent austenite. This is represented by incorporating the associated free energy change into ΔG_m. Buildup of carbon on the ferrite/austenite interfaces contributes to a drop in local driving force for nucleation on previously formed ferrite plates (auto-catalysis). An auto-catalysis factor β is defined that is empirically related to the mean concentration of the alloy. The effect of auto-catalysis is then modelled by equation

3.13.

$$I = I_\circ \left(1 - \beta\theta\xi\right) \tag{3.13}$$

The overall growth rate is given by

$$\frac{\mathrm{d}\xi}{\mathrm{d}t} = \frac{uK_1}{\theta}\left(1 - \xi\right)\left(1 + \beta\theta\xi\right)\exp\left[-\frac{K_2}{RT}\left(1 + \frac{\Delta G_m^\circ}{r}\right) + \Gamma\xi\right] \tag{3.14}$$

where Γ is given by equation 3.15.

$$\Gamma = \frac{K_2\left(\Delta G_m^\circ - G_N\right)}{rRT} \tag{3.15}$$

The above model assumes that carbon that diffuses out of the ferrite plates is uniformly distributed within the remaining austenite, which is not entirely true. Some of the austenite, supersaturated with carbon, remains in the form of isolated films between ferrite plates [65]. Para-equilibrium conditions are assumed, and so the carbon composition of the austenite films is arrived at by thermodynamic equilibrium calculations.

Diffusional Theory

In the diffusional theory of bainite transformation, the formation of bainite takes place through a random walk of atoms across the phase interface, with a bias towards the product phase. The bainite reaction is considered as a competitive eutectoid reaction, as opposed to a cooperative eutectoid transformation such as pearlite [48]. Proponents of the diffusional theory cite experimental evidence [67, 68] to support the lengthening and thickening of bainite plates at diffusion controlled rates. Specifically, the diffusion

25

of carbon in austenite is most likely the rate determining mechanism [53]. Furthermore, experimental evidence is referred to where bainite plates have been observed to grow continuously, which would not be compatible with the step-wise growth suggested by the displacive theory of transformation [69].

The dominant effect on the driving force available for nucleation is that of the interfacial energy; in order to minimize the interfacial energy, the critical nuclei of a precipitate must be as coherent as possible with the matrix, resulting in nucleation with detectable kinetics, and prejudicing growth towards partial coherency [70]. However, once beyond the nucleation stage, growth of the precipitated phase is influenced more by the orientation dependence of the ferrite-austenite boundary mobility [48]. Precipitated crystals can be enclosed entirely by full or partially coherent boundaries. Given that the stacking sequence on the two sides of these boundaries is different, the boundaries are entirely immobile in the direction normal to themselves [54]. Misfit dislocations exist at the interphase, and measurements and observations suggest that these dislocations are sessile [71]. The ferrite-austenite boundaries must therefore be displaced through the ledge mechanism [48], where plate growth is achieved through lateral diffusional migration of the ledges. This is in direct conflict with the displacive theory, which holds that the interphase is glissile.

According to authors advocating the diffusional mechanism of transformation, there is no fundamental difference in the mechanism of formation of Widmanstätten ferrite, upper bainite and lower bainite; at temperatures where bainite forms, there is no break in the edgewise growth rate as undercooling increases that would indicate a change of mechanism. Also, the edgewise growth of ferrite plates is too slow to cause carbon supersaturation in the ferrite [72].

The surface relief effect which is cited as a major piece of evidence by displacive theory advocates is questioned by Aaronson and co-workers [54]. Indeed, it is claimed by the diffusive camp that bainite formation does not

fulfil the phenomenological theory of martensite crystallography (PTMC), which is necessary for a displacive mechanism (the sessile austenite-ferrite interfaces being one violation of PTMC). Furthermore Muddle et al.[73] claim that PTMC is not a reliable indicator of a martensitic type of transformation. Aaronson et al.[74] point out that some diffusional phase transformation have crystallography that is predictable by PTMC due to the fact that their habit planes appear to be invariant planes. The displacive theory's treatment of the incomplete transformation phenomenon is also questioned; by the diffusional theory, it is possibly due to a solute drag like effect [46].

Hillert [75] states that there is no clear signs of carbon supersaturation in bainitic ferrite during growth, and that kinetic indications exist that show that the ferrite/austenite interface is not closely related to interface features present in lath and plate martensite. In more recent work, Hillert and co-workers cite new metallographic evidence of carbon diffusion during ferrite growth [76]. They are convinced that Widmanstätten ferrite and the ferritic portion of bainite are the same structure [56].

Several authors have presented approaches to modelling the growth of plates by diffusion [77, 78, 79, 80, 81, 82]. A fairly recent model by Quidort and Brechet [53] expands upon the method used by Trivedi [81] where a simplified expression is used for the growth rate, assuming infinite mobility of the interface and neglecting capillary effects. The growth rate v is given by the solution of an expression of the dimensionless Peclet number p given by equation 3.16.

$$p = \frac{9}{16\pi}\Omega_*^2 = \frac{\rho v}{2D_C} \qquad (3.16)$$

where ρ is the curvature at the plate growth tip, D_C is the diffusivity coefficient of carbon in austenite, and Ω_* is an algebraic combination of the solute supersaturation in austenite, and is given by

$$\Omega_* = \frac{\Omega_\circ}{1 - 2\frac{2}{\pi}\Omega_\circ - \frac{1}{2\pi}\Omega_\circ^2} \tag{3.17}$$

The solute supersaturation in austenite is defined as:

$$\Omega_\circ = \frac{x_C^{\gamma\alpha} - \bar{x}_C}{x_C^{\gamma\alpha} - x_C^{\alpha\gamma}} \tag{3.18}$$

The variables $x_C^{\gamma\alpha}$, $\bar{x}_C$, and $x_C^{\alpha\gamma}$ represent the atomic fraction of carbon in austenite at the interface, the average atomic fraction of carbon, and the atomic fraction of carbon in ferrite at the interface respectively. The values of $x_C^{\gamma\alpha}$ and $x_C^{\alpha\gamma}$ are calculated assuming para-equilibrium at the ferrite/austenite interface. The assumption is made that the system selects a critical tip curvature ρ_C that gives the maximum rate of growth $v_\circ$. Then,

$$v = v_\circ = \frac{27D\Omega_*^3}{256\pi\rho_C} \tag{3.19}$$

The authors include an adjustment of the carbon concentrations at the interface to account for an acceleration due to cementite precipitation based on a mass balance at the ferrite/austenite interface. They find, however, that the model predicts transformation rates significantly higher than shown by experimental data. They suggest that interaction of substitutional elements with the moving interface must be causing a solute drag like effect. They also suggest that the simplified thermodynamic conditions at the interface which were assumed for the model are not sufficiently accurate, and that for a general case, concentrations at the interface should be calculated with consideration of several interacting processes such as diffusion of several different elements, solute drag, and the FCC to BCC atomic rearrangement.
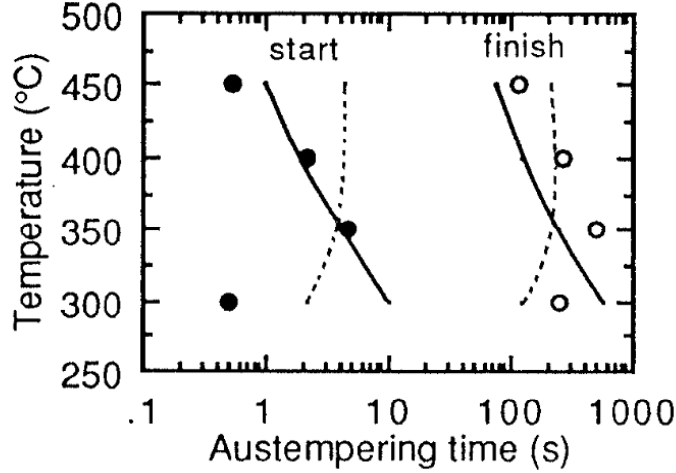
Figure 3.7: Dependence of bainite start and finish on austempering temperature. Solid lines show predictions calculated by the diffusional model, dotted lines show predictions calculated by the displacive model. TRIP steel (Fe-0.19C-1.45Si-1.54Mn-0.032Al wt%)[1][83].

Minote et al.[83] examined bainite transformation in TRIP steel. Samples were austempered at temperatures between 300°C and 450°C and the bainite transformation was observed. The authors found that neither the diffusional, nor the displacive theory described the bainite transformation start and finish times over the entire temperature range. Rather, the diffusional theory was found to be sufficient above 350°C while the displacive theory performed better below. A summary of these results can be seen in figure 3.7.

3.3 The Role of Niobium

One of the main goals in thermomechanical processing of micro-alloyed steels is to achieve a fine microstructure in the final product. Higher strength and

---

[1]Original published in ISIJ International.

greater resistance to brittle fracture are two of the important benefits afforded by smaller grain sizes [84]. The addition of micro-alloying elements such as titanium, niobium, aluminum, and vanadium is a common method of increasing the strength and brittle fracture resistance of steels through refinement of the final microstructure, achieved through the prevention or retardation of austenite recrystallization after deformation, or austenite grain growth during the reheat stage. Furthermore, an even distribution of fine stable carbonitride particles can be achieved during thermomechanical processing that serves to strengthen the steel [1]. Niobium in solid solution and niobium carbonitride precipitates have a significant effect on the condition of austenite [1, 84, 85, 86, 87, 88, 89], and on the nucleation and growth of the product phases [1, 90, 91, 92, 93, 94]. It is thus a very common micro-alloying element in low alloy steel grades with applications ranging from automotive to oil and gas line-pipes. Niobium is an alloying element in the steel studied in this work; a brief review has therefore been made of its role in the thermomechanical processing of micro-alloy steels.

3.3.1 Niobium Precipitation and Interaction with Austenite Recrystallization

At equilibrium, the concentrations of niobium present in austenite either as a solute in the matrix or in precipitate form can be calculated using the solubility product of niobium carbonitride in austenite [1]. The solubility product can be derived using thermodynamic calculations, or experimentally, and will vary with the alloy composition. The precipitation of niobium carbonitride is heterogeneous in nature, and will typically occur at crystalline defects such as grain boundaries, incoherent twin boundaries, sub-grain boundaries, and dislocations. Interphase precipitation can also take place during the austenite to ferrite transformation; precipitates form on the advancing boundary between austenite and ferrite, and are left behind in the ferrite as the boundary passes [1, 95].
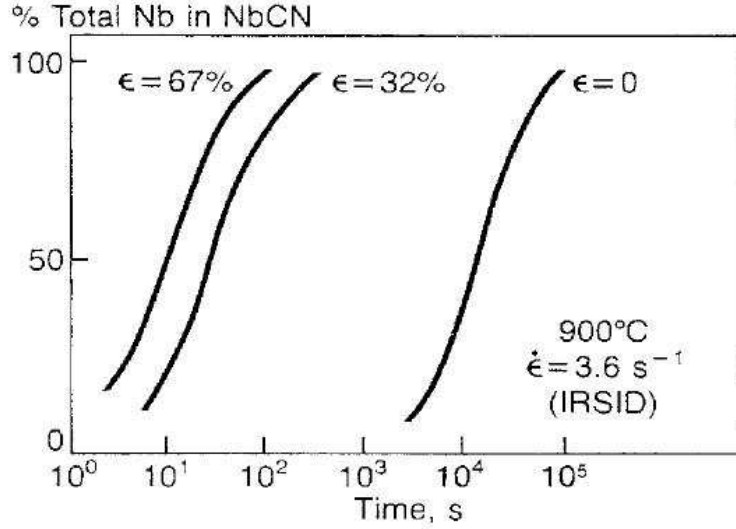
Figure 3.8: Effect of deformation on precipitation kinetics [2]

The kinetics of precipitation of niobium carbonitrides in micro-alloyed austenite is typically rather sluggish due to the close proximity to the solvus while in the austenite phase field [1]. However, the introduction of deformation promotes nucleation of precipitates by increasing the availability of potential nucleation sites, which is of great significance in thermomechanical processing. This is demonstrated in figure 3.8 for a steel with alloy composition (in wt%) of 0.17C-0.04Nb-0.011N[2].

Palmiere et al.[84] determined that localized precipitation of Nb(CN) was greater at favoured nucleation sites than in the bulk of the matrix by a factor of $1.5 - 2$. Speer and Hansen [86] concluded that strain induced precipitation of niobium carbonitrides occurs in two stages. During the first stage, immediately after deformation, precipitates nucleate at grain boundaries and deformation bands. The second stage of precipitation occurs within grains. Should recrystallization precede the second stage of Nb(CN) precipitation, precipitation will occur in the matrix at a sluggish rate. However, if precipitation occurs before recrystallization, nucleation of Nb(CN) particles occurs
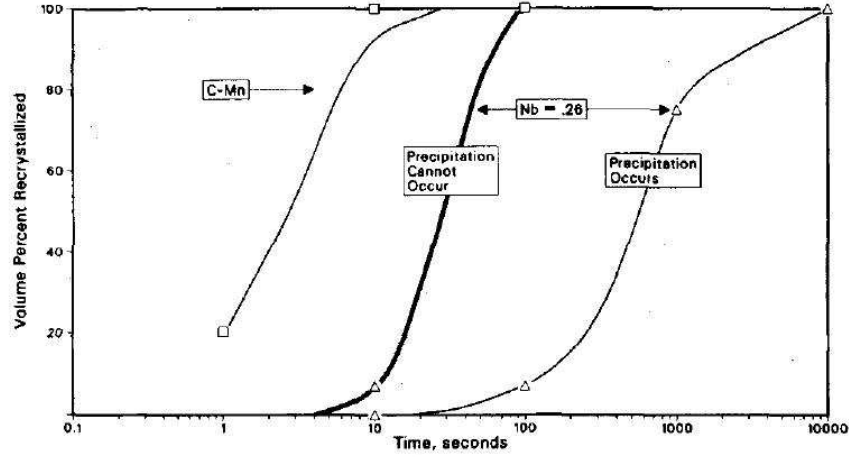
31

Figure 3.9: Effect of niobium on austenite recrystallization for a deformation temperature of 954°C.[86].

on the sub-grain boundaries within unrecrystallized grains. The fine dispersion of particles thus formed is capable of providing recrystallization growth retarding forces comparable in magnitude to the driving force for recrystallization. Essentially, Nb(CN) precipitation and austenite recrystallization are coupled. The formation of fine precipitates promoted by the substructure of deformed, unrecrystallized austenite serves to retard or temporarily halt the recrystallization process through grain boundary pinning [1, 84, 85, 86, 87].

The effect of the presence of Nb(CN) precipitates on recrystallization can be seen in figure 3.9. In the figure, the curve to the far left belongs to a steel with composition (in wt%) of 0.087C-1.90Mn-0.23Si. The middle and right curves belong to a steel with composition (in wt%) of 0.012C-1.98Mn-0.28Si-0.11N-0.26Nb. Recrystallization occurs rapidly in the C-Mn steel. In the case of the far right curve, labelled "Precipitation Occurs," all of the niobium is in solution prior to deformation, and thus precipitation of fine Nb(CN) is induced by deformation. The middle curve, labelled "Precipitation Cannot Occur" represents the case where Nb(CN) precipitation and

32

coarsening has been permitted prior to deformation, such that niobium in the austenite has equilibrated. By "Precipitation Cannot Occur" it is meant that no precipitation occurs during deformation, as all Nb(CN) that could have precipitated during deformation is already in precipitate form.

Refer to the far right curve in figure 3.9. The deformation-induced precipitation of niobium carbides significantly retards recrystallization, such that it is not complete until 10^4 seconds have passed. Where particles are coarse and wide-spaced, they have little effect on the recrystallization behaviour in the steel; however observing the middle curve in the figure, it can be seen that despite the lack of effective precipitates, recrystallization kinetics in the Nb steel are still slower than they are in the C-Mn steel. In order to explain this, it must be noted that the niobium content of the steel is quite high relative to its carbon content (0.26wt% Nb versus 0.012wt%C): A large proportion of the niobium in the steel remains in solution throughout the process. The slower recrystallization kinetics relative to that of the C-Mn steel is explained by the solute drag effect of niobium on the migrating grain boundaries [1, 85, 86].

Conclusions from figure 3.9 can be summarized as follows: Although both solute atoms and precipitates can suppress recrystallization, fine precipitates are far more effective at slowing recrystallization than solute atoms. In the steel shown in the figure, the precipitation of 0.01wt% of the niobium dissolved in the steel as carbonitrides on the substructure of deformed the austenite (far right curve), prior to recrystallization, was more effective at suppressing recrystallization than keeping 0.20wt% niobium in solid solution (middle curve)[86].

3.3.2 Effect of Niobium on the Austenite to Ferrite Transformation

Niobium carbonitride precipitates serve as additional nucleation sites for ferrite, in polygonal, acicular or bainitic morphologies. Furthermore, their exis-

tence tends to raise transformation start temperatures and thus promote the growth of higher temperature transformation products [1, 90, 91, 92, 93]. It has been suggested that the presence of fine deformation induced precipitates could later serve to slow the reaction through a boundary pinning mechanism [93] or through changes in local matrix chemistry and carbon fluxes caused by precipitation process. A recent study by Bréchet and co-workers [96] points to the contrary, however; in contrast to their appreciable effect on grain boundary motion, niobium carbonitride precipitates did not discernibly effect the motion of the interphase during the austenite to ferrite transformation.

Niobium in solid solution in austenite tends to suppress ferrite formation [1, 90, 91, 92, 93]. As the concentration of niobium in solution increases, transformation start temperatures are lowered, and the transformation proceeds at a slower pace. The hardenability of micro-alloyed steels containing niobium can therefore be increased by dissolving a greater portion of niobium prior to transformation. The reduction in kinetics is more pronounced at lower cooling rates, where the driving force for transformation is low [91]. Figure 3.10 shows the effect of increasing amounts of niobium in solution on the transformation rate during an isothermal treatment at 670°C; varying amounts of niobium in solution were achieve by holding samples for a range of holding times at 900°C.

There seems to be a lack of consensus on the mechanism by which niobium in solid solution suppresses the austenite to ferrite transformation. While some authors propose a solute drag mechanism on interphase boundaries [94, 93], others reject this [90, 91]. Authors who disagree with the solute drag mechanism propose the following: The misfit strain around niobium atoms that have segregated to austenite grain boundaries interact with and lower the surface energy of grain boundaries, and thus reduce the potency of nucleation sites. Additionally, niobium solute atoms at grain boundaries might be interacting with carbon atoms, either lowering the driving force
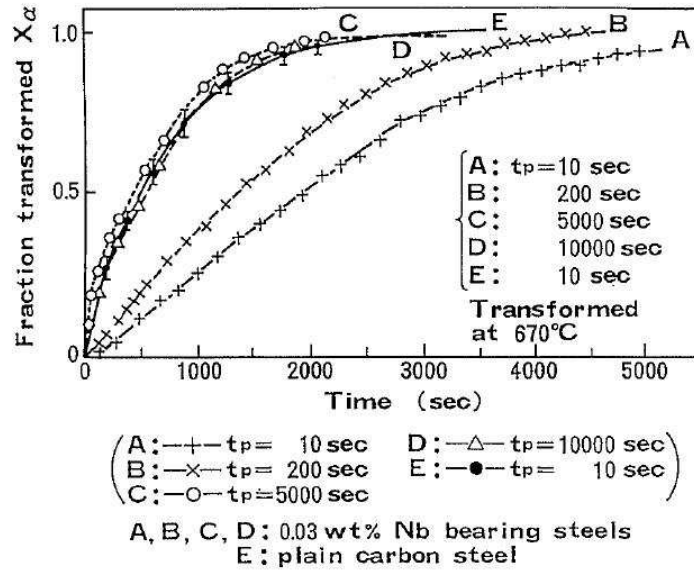
Figure 3.10: Effect of Nb in Solution on Transformation[2] [4]

for ferrite formation, or limiting the diffusion of carbon away from ferrite nuclei[90].

The solute drag theory is rejected by proponents of the displacive formation theory for bainite. The presence of niobium solutes delays the onset of bainite formation; the diffusional solute drag theory is incompatible with the displacive mechanism[90].

---

[2]Original published in ISIJ International.

Chapter 4

Experimental Methodology

4.1 Materials

The experimental work was carried out on a low-carbon line-pipe grade steel sample provided by Essar Steel Algoma (see Table 4.1 for composition).

Table 4.1: Composition of sample steel (wt %)

C	Mn	S	P	Si	Nb
0.06	1.49	0.002	0.009	0.2	0.047

Al	Cr	Cu	Ti	V	N
0.038	0.02	0.02	0.001	0.003	0.0094

The dependence of the transformation behaviour of the steel on austenite grain size, retained strain, and cooling rate was investigated by conducting Continuous Cooling Transformation (CCT) tests. CCT tests were also used to evaluate the effect of niobium dissolution in austenite on austenite decomposition. In brief terms, the tests involved samples being machined from the above steel, austenitized, deformed, and cooled using different reheat conditions, strain levels, and constant cooling rates.

Designing the CCT test regimes required data on austenite grain growth

during the reheat stage, and austenite softening behaviour following deformation. Preliminary experiments were therefore carried out prior to designing the CCT tests in order to generate the aforementioned data. They are discussed in the following sections.

4.2 Simulations

4.2.1 Apparatus

All simulations were carried out on a Gleeble 3500 Thermomechanical Simulator. Samples were held in water cooled copper grips, and heated resistively using an adjustable electrical current. Temperature control was achieved by varying the current passing through the samples according to feedback from a thermocouple welded on to the surface of the sample. For cooling regimes requiring high cooling rates, either compressed helium gas or water was used as a quench medium. A computer controlled hydraulic system applied compressive strain to the sample through the sample grips. Simulations were conducted either under vacuum (10^{-4}torr/0.013Pa) or in an argon atmosphere.

A dilatometer was used to measure diametric dilation of the sample during the simulation. A strain measuring device was substituted for cases where sample strains exceeded the range limits of the dilatometer and high sensitivity was not required.

4.2.2 Austenite Grain Growth Tests

Rectangular test samples measuring 3mm x 6mm x 15mm were machined from the provided steel plate. See figure 4.1. Prior to each test, a Pt/Pt-Rh thermocouple was welded at the sample surface.

The samples were heated at 5°C/s to specific austenitizing temperatures and held there for a period of 5 minutes to allow for grain growth, after
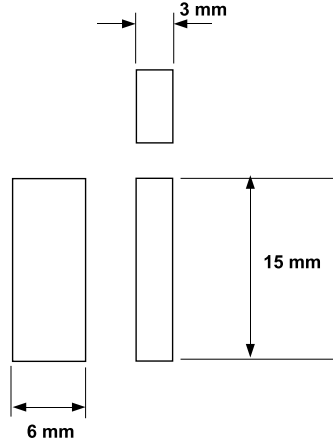
Figure 4.1: Austenite grain growth test sample geometry

which time they were water-quenched to room temperature. The range of austenitizing temperatures used was 950°C to 1250°C, with tests carried out at 50°C increments.

The prior austenite grain size was measured using image analysis. In order to improve the definition of the prior austenite grain boundaries, the samples were annealed at 550°C for 24 hours in an argon atmosphere furnace. The samples were then sectioned, ground, polished and etched using a saturated aqueous picric acid solution (see table 4.2 for etchant details). Photomicrographs of random locations on the etched samples were generated using an optical microscope. The prior austenite grain boundaries where then highlighted, and Clemex image analysis software was used to measure the average prior austenite grain size (EQAD), according to procedures outlined in ASTM standard E 1382-97 [1].

---

[1]E 1382-97: Standard test methods for determining average grain size using semi-automatic and automatic image analysis; ASTM International, 2004.

Table 4.2: Etchants used for metallography

Use	Etchant and Composition	Notes
Revealing prior austenite grain boundaries	- 100mL Saturated Aqueous Picric Acid - 80 mg $CuCl_2$ - 3 mL Wetting Agent	Swab sample surface with NaOH after etching
Revealing ferrite/ferrite and ferrite/cementite boundaries	2% Nital - 98 mL Ethyl Alcohol - 2 mL Nitric Acid	
Revealing martensite/ retained austenite	LaPera's Etchant Equal Proportions of: - 4g Picric Acid + 100mL Ethyl Alcohol - 1g Sodium Metabisulphate + 100 mL Water	

4.2.3 Austenite Softening Tests

The experiments conducted to investigate austenite softening behaviour followed established procedures for "Double-Hit" tests: Cylindrical samples 1cm in diameter and 1.5cm in length were machined from the sample material. A Pt/Pt-Rh thermocouple was welded to the surface of each sample. Samples were then mounted in the Gleeble between hydraulically operated anvils. A diametric strain gauge was used to measure the strain in the sample, a load cell in line with the sample was used to measure compressive forces applied on the sample. See figure 4.2a for sample geometry.

The samples were heated and held at austenitization temperatures according to the selected reheat regimes discussed above, then cooled to 850°C at 10°C/s. Once the samples' temperatures were stabilized for 2 seconds at 850°C, they were subjected to a strain of 0.3 at $1s^{-1}$ in the first "hit." Following several different holding times (5 through 60 seconds), the samples were strained again in a second "hit", this time past their yield point. See figure 4.2b for a schematic diagram of the test regime.
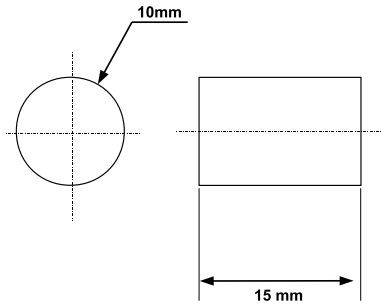
(a)
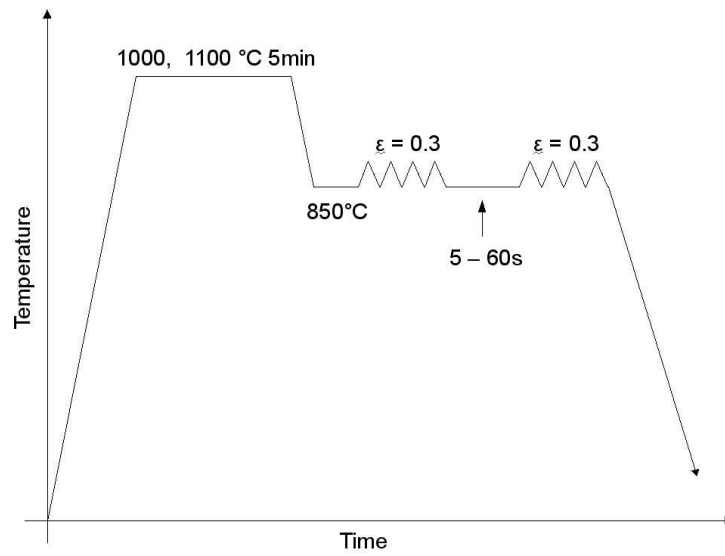
(b)
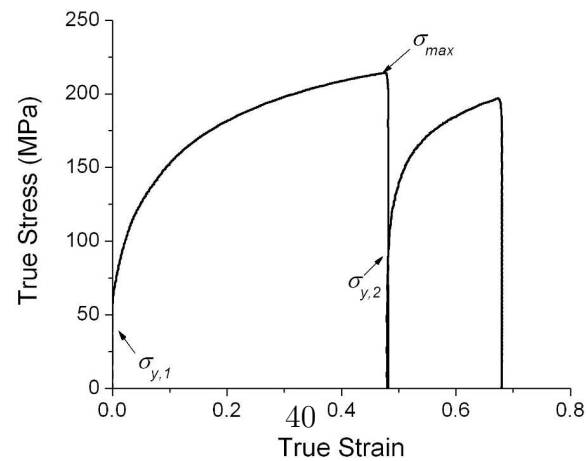
(c)

Figure 4.2: Double hit test. (a) Sample geometry, (b) Test regime, (c) example of results

Values for true stress and true strain were calculated for each sample using load and deformation data acquired during each test. The yield stress at each 'hit' was defined as the stress at an offset strain of 0.002. The degree of softening in a sample was defined by:

$$\text{Softening} = \frac{\sigma_{max} - \sigma_{y,2}}{\sigma_{max} - \sigma_{y,1}} \quad (4.1)$$

where $\sigma_{y,1}$ and σ_{max} are the yield stress and maximum stress during the first hit, and $\sigma_{y,2}$ is the yield stress during the second hit. The variables σ_{max}, $\sigma_{y,1}$, and $\sigma_{y,2}$ are shown in figure 4.2c.

4.2.4 Continuous Cooling Transformation Tests

The data generated in the experiments described above were used to determine the appropriate regimes for the CCT tests. Schematics of the test regimes can be seen in figure 4.3a. The samples were heated to 1000°C or 1100°C, cooled at 10°C/s to 850°C, left undeformed or deformed to a strain of 0.3 or 0.6 at $1s^{-1}$ and the immediately cooled at 50°C/s to 800°C to avoid softening in the deformed samples. The samples were then cooled to room temperature at constant cooling rates of 1°C/s to 50°C/s.
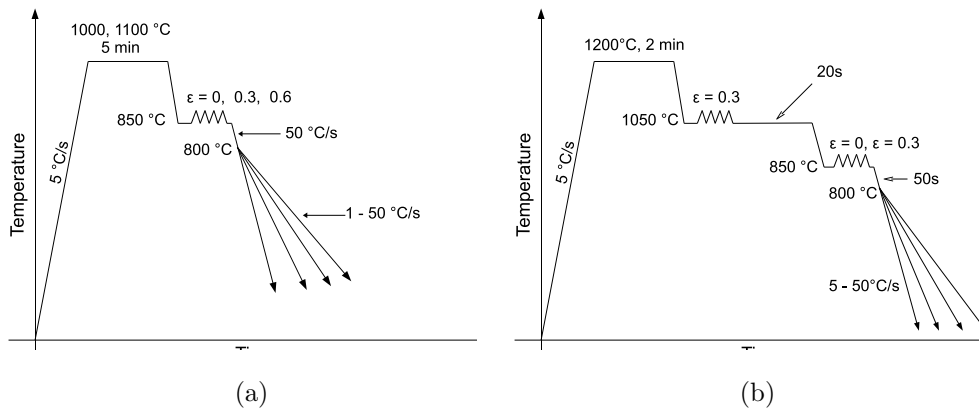

Figure 4.3: Test regimes. (a) CCT (b) Nb-in-solution CCT regime

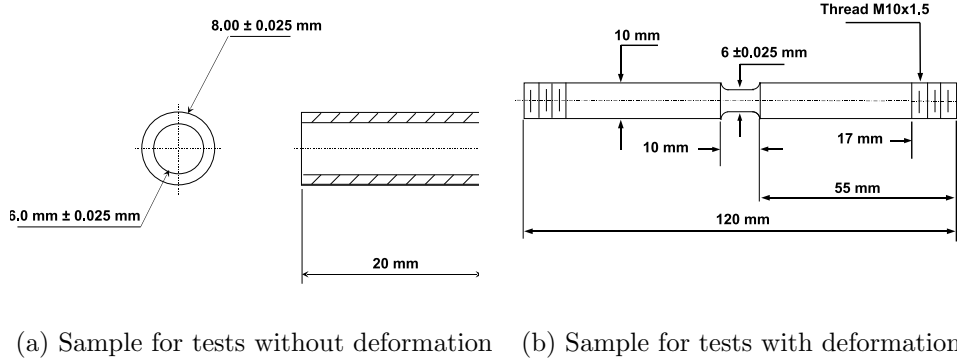(a) Sample for tests without deformation   (b) Sample for tests with deformation

Figure 4.4: CCT test samples

Two different sample geometries were used: Hollow cylindrical tubes for tests that did not require deformation (figure 4.4a), and solid cylindrical bars for tests that required deformation (figure 4.4b).

Niobium Dissolution Continuous Cooling Transformation Tests

Investigating the effect of niobium dissolution on the transformation behaviour of the steel required changes to the established CCT test procedures explained above.

It was determined that 1 minute at 1200°C was sufficient to dissolve all niobium carbonitride precipitates [97]. In order to assure full dissolution of niobium, a hold time of 2 minutes at 1200°C was selected. The austenite grain growth data for the steel showed however that this would result in a large austenite grain size in excess of $100\mu m$, and would not be reflective of industrial conditions. A grain refining step was therefore introduced: Once the niobium dissolution procedure was complete, samples were cooled at 10°C/s to 1050°C and subjected to a strain of 0.3 at a rate of $1s^{-1}$ in order to induce recrystallization of the austenite grains. Once deformed, the samples were held for a predetermined period of time to allow for full recrystallization

of the austenite grains. The samples were then either cooled at 50°C/s to 850°C, left undeformed or subjected to a strain of 0.3 at a rate of $1s^{-1}$, then cooled at 50°C/s to 800°C to avoid softening. All samples were then cooled to room temperature at constant cooling rates between 5°C/s and 50°C/s. A schematic of the test regime can be seen in figure 4.3b.

The time for full recrystallization was determined from double hit tests at 1050°C. Assuming that 100% softening corresponded to a fully recrystallized condition in the austenite, an optimal holding time at 1050°C.

Several niobium-in-solution CCT samples were water quenched immediately after the recrystallization step and etched with a picric acid solution to reveal the recrystallized austenite grains. The recrystallized grain size was then measured by image analysis using the same methods as previously described.

Data Processing

During cooling, dilation data acquired during each test were plotted against the corresponding sample temperatures. See figure 4.5a for an example. Two linear portions can be seen in the plot. The linear region at higher temperatures shows the thermal contraction of the sample in the austenitic region, while the linear region at lower temperatures shows that in the ferritic region. The transition region between the two linear regions corresponds to the transformation of the austenite FCC structure to BCC structure in the ferrite; the expansion of the sample in this region is associated with the greater atomic volume of the BCC structure relative to the FCC structure. This transition region was used to track the decomposition of the austenite through a simple application of the lever rule (figure 4.5a). Figure 4.5b shows an example of a transformation curve calculated from dilation and temperature data.

Analysis of the transformation dilation data was supplemented by quantitative analysis of sample microstructures. Each sample was sectioned,
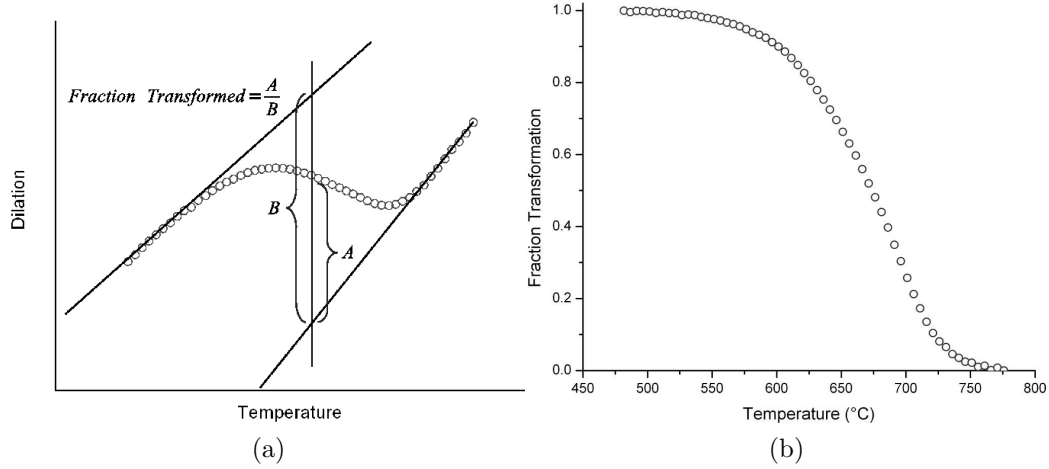
Figure 4.5: CCT dilation data processing: Dilation data and lever rule (a); calculated CCT transformation curve (b).

polished, and etched in a 2% nital solution to delineate ferrite/ferrite and ferrite/cementite boundaries to allow identification of ferrite and bainite. Optical micrographs of the etched surfaces were used to measure the fraction of ferrite in each sample, using the point count method outlined in the ASTM standard E 562. The samples were then re-polished and etched once more, this time in LePera's solution, revealing regions of martensite/ retained austenite (MA). Image analysis software was used to measure the fraction of MA in each sample. The remaining fraction of the microstructure in each sample was considered to be bainite.

Chapter 5

Results and Data Analysis

5.1 Preliminary Test Results

Austenite Grain Growth

A brief study of austenite grain growth was conducted on the steel in order to determine the appropriate reheat conditions for the CCT tests. Observation of the austenite grain growth test samples revealed a range of average equivalent austenite grain diameters D_γ (EQAD) between 10μm and approximately 150μm for 5 minute holding times between 1000°C and 1250°C. Image analysis was carried out on samples showing austenite grain sizes relevant to industrial processes (10 - 40μm).

Figures 5.1a and 5.1b show the distribution of EQAD's for holding temperatures of 1000°C and 1125°C respectively. Increasing the holding temperature resulted in larger austenite grain sizes. This trend can be seen in figure 5.1c, which shows the mean EQAD's for the reheat temperatures analysed. The trend resembles an exponential function. It was observed that greater reheat temperatures gradually shifted the grain size distributions away from normality; a 'tail' developed in the grain size histograms, due to the onset of abnormal grain growth.
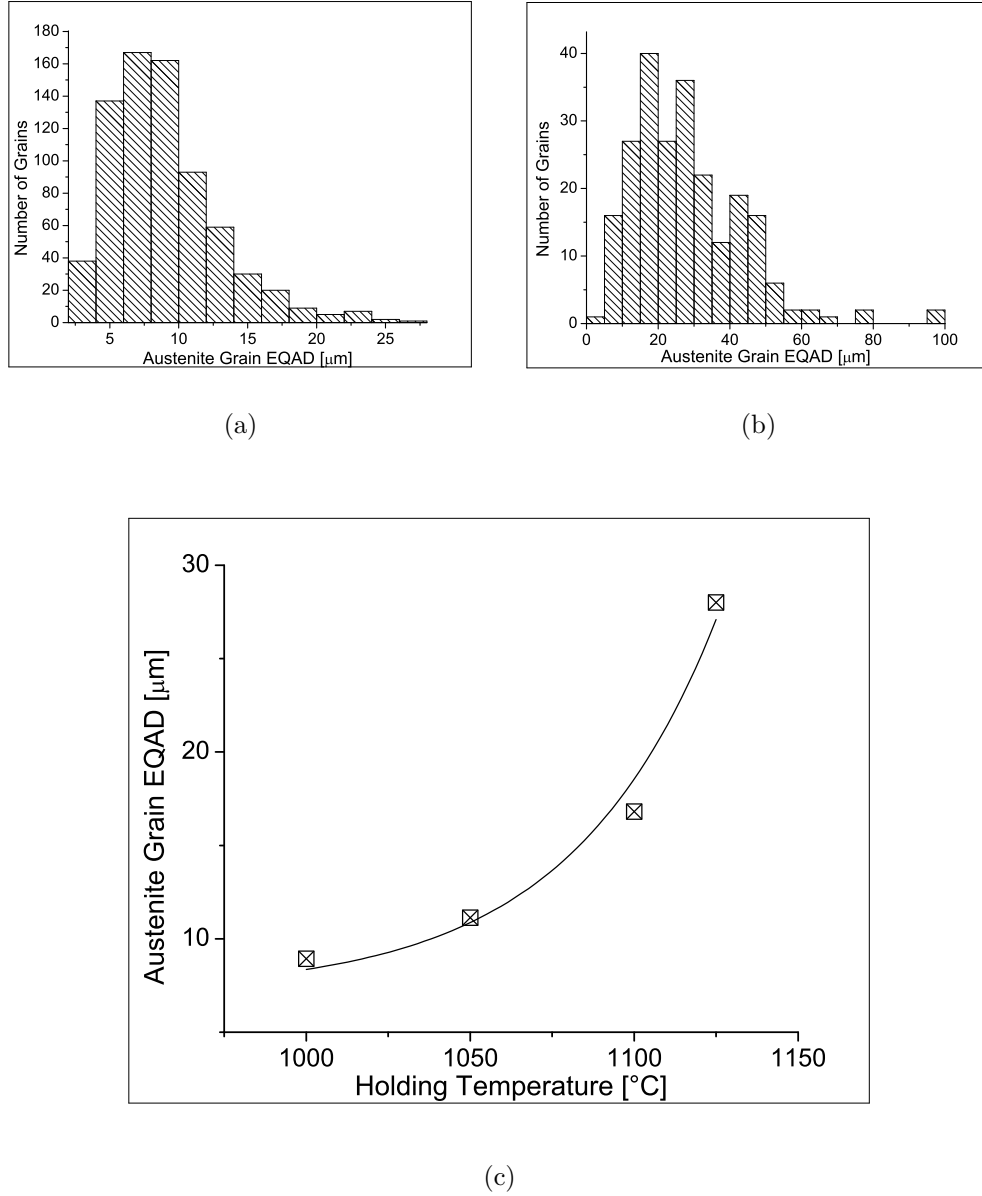
(a)

(b)

(c)

Figure 5.1: Austenite grain size distributions after 5 min at 1000°C (a), 1125°C (b). Mean grain diameter for range of holding temperatures plotted in (c).

Reheat conditions were selected for the CCT tests that produced sufficiently uniform austenite grain size distributions: 5 minutes at 1000°C and 5 minutes at 1100°C, resulting in mean D_γ's of 10μm and 17μm. Attempts to produce D_γ's beyond 17μm by adjusting the holding time and/or temperature failed to produce sufficiently uniform grain size distributions.

Austenite Softening

Recrystallization in austenite following deformation during CCT simulations was of concern; it was necessary to preserve the flattened austenite grain structure in order to measure the effect of retained strain on phase transformation behaviour in the steel. Softening following deformation is a direct consequence of recovery and recrystallization. "Double-Hit" tests measuring the degree of softening (as described in the preceding chapter) were utilized to investigate recrystallization kinetics in the steel. The calculated results can be seen in figure 5.2. The initial 10 - 20 % of the softening was assumed to be due to recovery, while the remainder was attributed to recrystallization [98].

Samples with an initial average austenite EQAD of 17μm were somewhat more resistant to recrystallization in comparison to samples with that of 10μm. While the cause of this difference in recrystallization kinetics was not investigated in the present study, it was taken into consideration when designing the following CCT test procedures. It is likely that the finer austenite grains produced at 1000°C promoted recrystallization.

The Niobium-in-solution CCT tests included an additional grain-refinement step involving a strain of 0.3 at 1050°C, followed by holding at 1050°C for a predetermined time to allow recrystallization. The time required for recrystallization was determined by performing 'double-hit' tests, as described in the previous chapter. Test results suggested an optimum holding time of 20 seconds for full recrystallization.
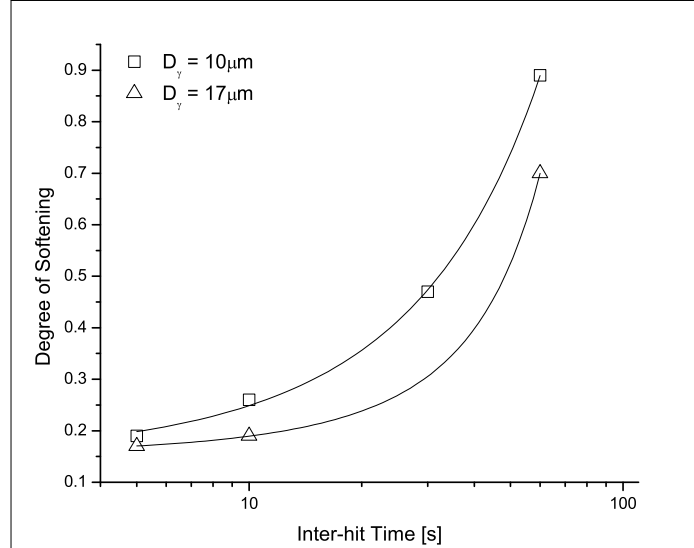
Figure 5.2: Austenite softening behaviour at 850°C, for initial γ - EQAD's of 10 and 17μm.

5.2 CCT Test Results

CCT tests were carried out for each of the 10 and 17μm initial grain diameters with three different levels of applied strain: $\epsilon = 0$, 0.3, and 0.6. Each initial austenite grain size and strain level was then subjected to cooling rates between 5 and 50°C/s.

It was not possible to separate the ferrite and bainite portions of the transformation using the dilation response of the sample. The transition from ferrite to bainite was smooth, and no transformation stasis was observed. The fraction of each constituent was instead measured through image analysis. However, the smooth transition complicated the image analysis also; identification of bainite was made difficult by the presence of highly non-polygonal ferrite phases that were at times indistinguishable from the bainite (see fig-

48

ure 5.3). An effort was made to remain consistent in identifying the phases, yet it was recognized that any measurements made would be approximate at best. An error of 10% in the measurement was considered appropriate.

It was assumed that all ferrite formed did so prior to the onset of pearlite and/or bainite formation. The final fraction of ferrite would therefore be present at the pearlite/bainite transformation start temperature, or equivalently the ferrite transformation stop temperature T_{fs}. The value of T_{fs} could then be approximated by comparing the fraction of ferrite in each sample measured by image analysis to the transformation curve of that sample calculated using its dilation response.

It was found that the decreasing the prior austenite grain size D_γ and increasing the amount of strain imparted on the austenite ϵ had similar effects on the transformation behaviour in the steel. An effective grain size D_{eff} was therefore introduced to combine the initial austenite grain size D_γ with strain ϵ, where [99]:

$$D_{\text{eff}} = D_\gamma \exp(-\epsilon) \tag{5.1}$$

Equation 5.1 can be applied under no-recrystallization conditions only. This was confirmed for the present CCT tests by austenite softening tests as discussed previously.

Effect of Cooling Rate

Transformation start temperatures T_s were lowered by as much as 59°C (for $D_{\text{eff}} = 17\mu$m), and ferrite stop temperatures T_{fs} were lowered by as much as 73°C (for $D_{\text{eff}} = 5\mu$m) as the cooling rate was increased from 5°C/s to 50°C/s. Plotting austenite fraction transformed vs temperature over the course of the transformation (figure 5.4), the effect of cooling rate on austenite decomposition can be seen clearly.
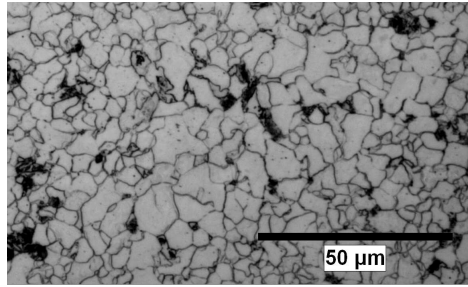
Metallographic observation of the test samples revealed that lower temperature transformation products were present in greater amounts at higher
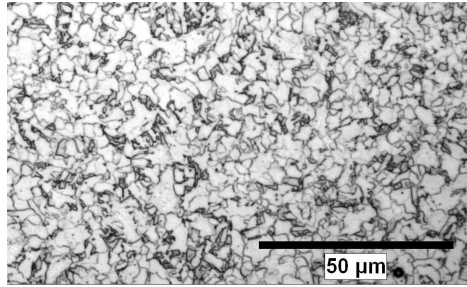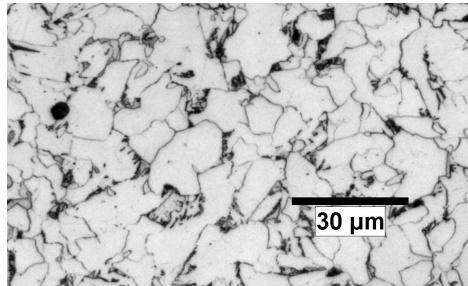
49
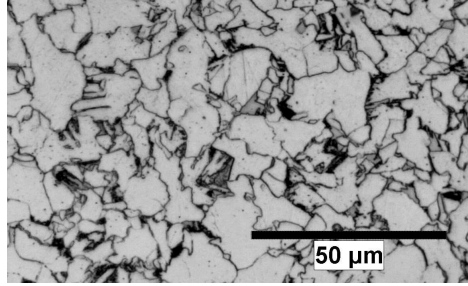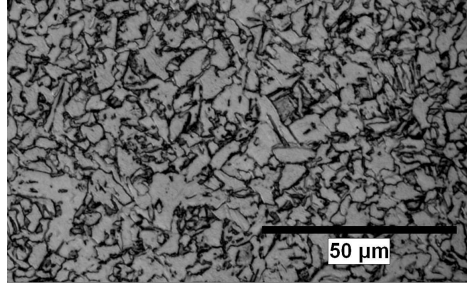
(a) $D_\gamma = 10\mu m$, $\epsilon = 0$, $q = 5°C/s$

(b) $D_\gamma = 10\mu m$, $\epsilon = 0$, $q = 50°C/s$

(c) $D_\gamma = 10\mu m$, $\epsilon = 0.6$, $q = 5°C/s$

(d) $D_\gamma = 10\mu m$, $\epsilon = 0.6$, $q = 50°C/s$

(e) $D_\gamma = 17\mu m$, $\epsilon = 0$, $q = 5°C/s$
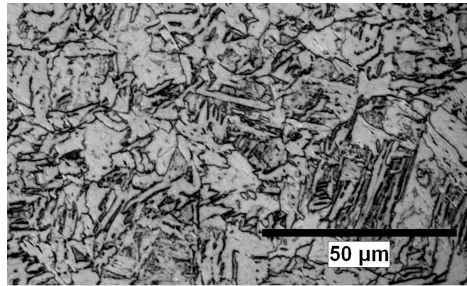
(f) $D_\gamma = 17\mu m$, $\epsilon = 0$, $q = 50°C/s$
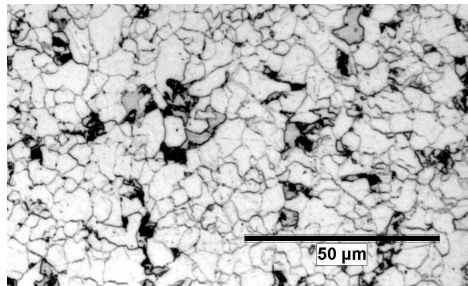
(g) $D_\gamma = 17\mu m$, $\epsilon = 0.6$, $q = 5°C/s$
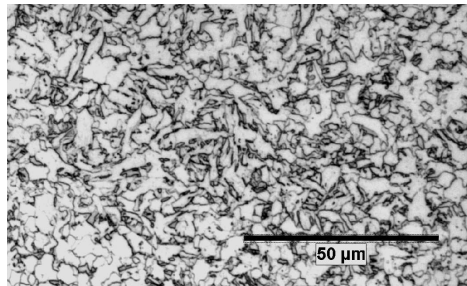
(h) $D_\gamma = 17\mu m$, $\epsilon = 0.6$, $q = 50°C/s$
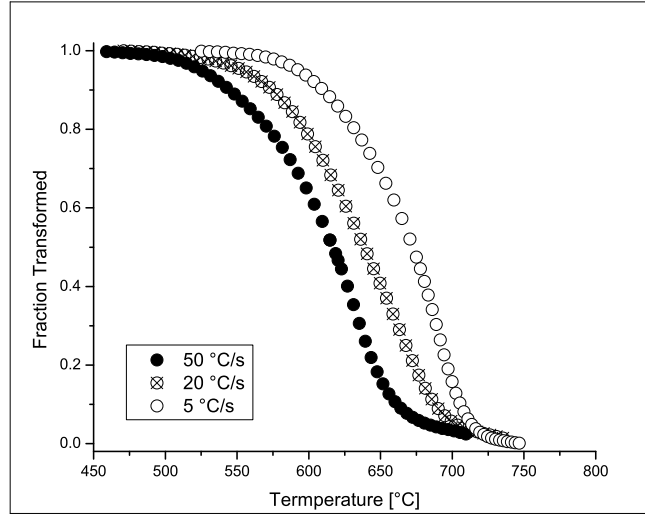
Figure 5.3: Photomicrographs of CCT samples, 2% nital etch

Figure 5.4: Effect of cooling rate on transformation for $D_\gamma = 17\mu$m and $\epsilon = 0$.

cooling rates; the fraction of polygonal ferrite decreased, as can be seen in figures 5.3a and 5.3f, and figures 5.3e and 5.3f. The photo-micrograph in 5.3e shows the microstructure resulting from cooling unstrained austenite with an average grain diameter of $17\mu m$ at a rate of 5°C/s. The product microstructure is composed primarily of polygonal ferrite (90%). Figure 5.3f shows the product of cooling austenite in the same condition as that of 5.3e at a rate of 50°C/s; in this case there is very little polygonal ferrite present, and the structure consists mainly of bainite(74%). The effect of cooling rate on the fraction of bainite was more pronounced in coarser, undeformed austenite grains. Deformation and austenite grain refinement seemed to reduce the effect of the cooling rate on the fraction of constituents formed.

In all cases, increasing the cooling rate refined the final microstructure. Figures 5.3c and 5.3d, shows the effect of cooling rate on the resultant microstructures of austenite with an average grain diameter of $10\mu m$ subjected

to a strain of 0.6, cooled at 5°C/s and 50°C/s, respectively. Although both cooling rates result in a microstructure consisting mainly of polygonal ferrite, increasing the cooling rate from 5°C/s to 50°C/s serves to refine the microstructure.

Etching the same samples to reveal martensite and retained austenite (M/A) showed an increase in the fraction of M/A with rising cooling rates. The M/A that formed under higher cooling rates was also finer and more evenly distributed.

Effect of Initial Austenite Grain Size

It was found that samples with $D_\gamma = 10\mu$m transformed at higher temperatures than those with $D_\gamma = 17\mu$m. Figure 5.5 shows austenite decomposition versus temperature for undeformed samples cooled at 50°C/s. The shift in transformation temperatures associated with a change in D_γ can be observed in the transformation curves. This change can be explained by noting the greater grain boundary area density in finer grained materials which serves to increase the availability of nucleation sites.

Higher transformation temperatures in samples with $D_\gamma = 10\mu$m resulted in greater fractions of polygonal ferrite. The effectiveness of lowering D_γ on increasing the fraction of ferrite was much more pronounced at higher cooling rates. Whereas the difference in the fraction of ferrite after cooling undeformed austenite at 5°C/s is essentially equivalent for both D_γ's - the difference in results is within experimental error - cooling undeformed austenite at 50°C/s resulted in an appreciable increase in the fraction of ferrite after a drop of D_γ from 17μm to 10μm: At $\epsilon = 0$ and $q = 50$°C/s, $X_f = 0.72$ for $D_\gamma = 10\mu$m, versus $X_f = 0.20$ for $D_\gamma = 17\mu$m. Respective photomicrographs are shown figures 5.3a and 5.3b.

Reducing the initial austenite grain also significantly increased the fraction of M/A in the samples; this was attributed to the greater carbon enrichment in untransformed austenite due to the early formation of greater
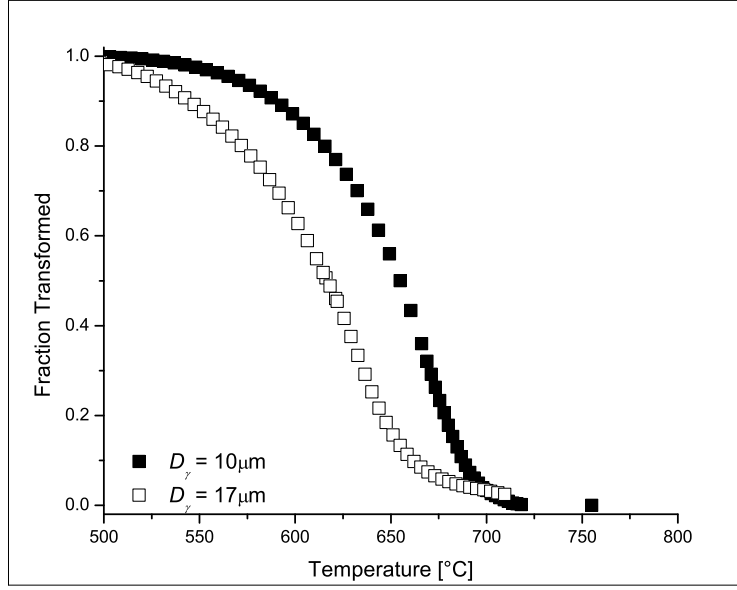
Figure 5.5: Effect of D_γ on transformation in samples with $\epsilon = 0$ and $q = 50°C/s$.

(a)   (b)
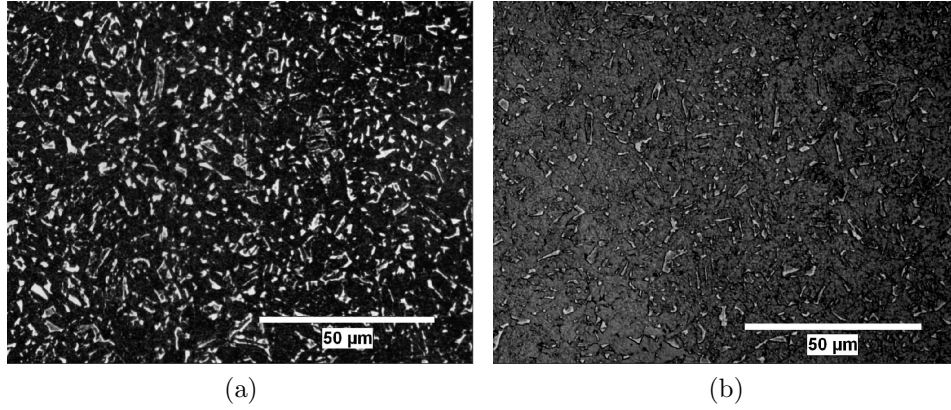
Figure 5.6: Photomicrographs of CCT samples for $\epsilon = 0$, $q = 50°C/s$, $D_\gamma = 10\mu m$ (a), and $\epsilon = 0$, $q = 50°C/s$, $D_\gamma = 17\mu m$ (b). LePera etch.

fractions of polygonal ferrite, and the lack of carbide precipitation which would have otherwise occurred during bainite formation [100]. Figure 5.6 shows an etch of undeformed samples with $D_\gamma = 10\mu$m and $D_\gamma = 17\mu$m, cooled at 50°C/s. The light phase is M/A and the dark background is ferrite and bainite. The figure shows a rather dramatic case of the effect of D_γ on the fraction of M/A: An M/A fraction of 0.06 for $D_\gamma = 17\mu$m and 0.11 for $D_\gamma = 10\mu$m, at an equivalent cooling rate, and no deformation.

Effect of Strain

Introducing strain in the austenite at 850°C (in effect flattening the austenite grains) shifted the transformation to higher temperatures. Much like reducing the initial grain size, introducing greater amounts of strain ϵ promoted the growth of finer, more polygonal ferrite, and suppressed the formation of bainite. The effect of ϵ on the start temperature and kinetics of transformation is illustrated in figure 5.7. The transformation curve is shifted to lower temperatures by up to 100°C.

Referring once more to figure 5.3 and comparing photomicrographs of samples with identical D_γ and q, the effect of introducing ϵ can be readily observed. Samples that have undergone deformation show finer, more ferritic microstructures. For the case of $D_\gamma = 17\mu$m and $q = 50$°C/s, the measured fraction of bainite decreased from 0.74 to 0.15 with the introduction of a strain of 0.6. The effect of ϵ on the fraction of bainite is more pronounced in samples with $D_\gamma = 17\mu$m, however the most fine, ferritic microstructure after $q = 50$°C/s ($X_f = 0.72$, $X_{M/A} = 0.11$) was achieved with $D_\gamma = 10\mu$m and $\epsilon = 0.6$.

Introducing ϵ from 0 to 0.6 doubled the fraction of M/A (from 0.06 to 0.12), in a manner similar to reducing D_γ (figure 5.8).

Table 5.1 shows a summary of test conditions and results. In the table, X_f, $X_{M/A}$, and X_{other} are the fractions of ferrite, M/A and 'other' constituents, respectively. The term 'other' used here is a feature of the methodology used
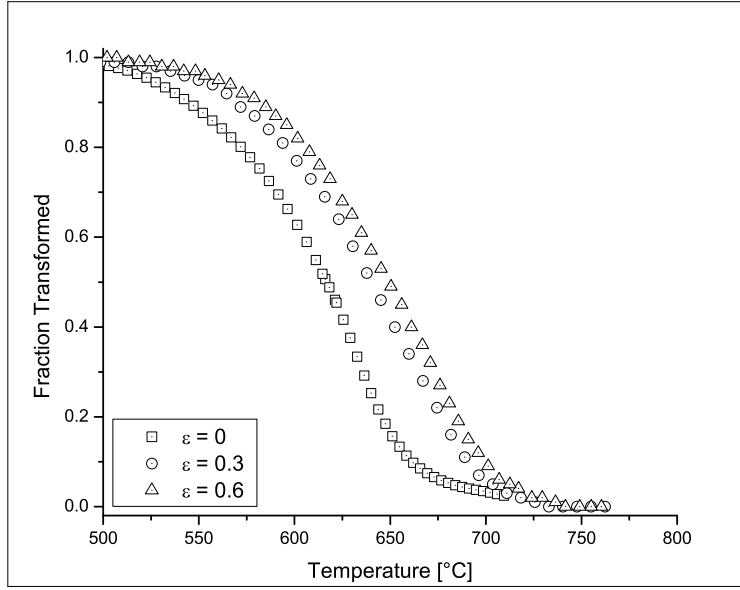
Figure 5.7: Effect of ϵ on transformation in samples with $D_\gamma = 17$ and $q = 50°\mathrm{C/s}$.
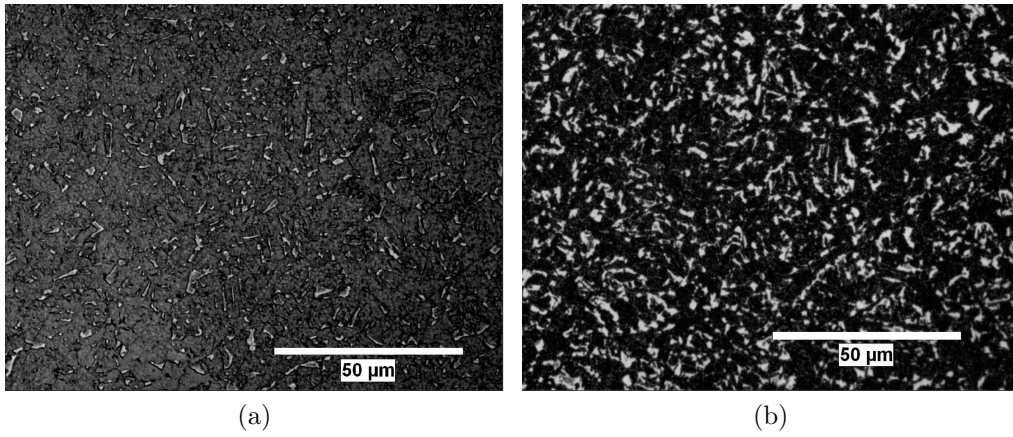

(a)   (b)

Figure 5.8: Photomicrographs showing the effect of ϵ on the M/A fraction (light phase) in samples with $D_\gamma = 17$, and $q = 50°\mathrm{C/s}$. (a) $\epsilon = 0$; (b) $\epsilon = 0.6$.

to measure the constituents. Ferrite and M/A were measured directly, while pearlite/bainite fractions were calculated as the remainder of the sample. It is assumed that pearlite constitutes the 'other' phase at transformation temperatures above $\sim 650°$C, while below it is assumed that bainite forms. Assuming that ferrite formed first in the absence of any other reactions, the temperature at which ferrite formation stopped in each sample T_{fs} was extracted from its transformation curve using its measured value of X_{f}.

The $\pm 10\%$ X_{f} measurement error is recorded in table 5.1. Note that it reflects in the values of X_{b}, and the extracted values of T_{fs}, also shown in the table.

Table 5.1: Results of quantitative image analysis

| D_{eff} (μm)	q (°C/s)	T_{s} (°C)	X_{f}	X_{b}	$X_{\text{M/A}}$	T_{fs}(°C)
5	5	771	0.84 ± 0.084	0.10 ± 0.084	0.06	714^{+10}_{-20}
5	20	745	0.83 ± 0.083	0.10 ± 0.083	0.07	656^{+16}_{-25}
5	50	734	0.75 ± 0.075	0.14 ± 0.075	0.11	651^{+13}_{-17}
7	5	768	0.85 ± 0.085	0.09 ± 0.085	0.06	712^{+9}_{-15}
7	20	746	0.79 ± 0.085	0.16 ± 0.085	0.05	675^{+10}_{-18}
7	50	721	0.59 ± 0.059	0.30 ± 0.059	0.11	662^{-9}_{-9}
9	5	762	0.89 ± 0.089	$0.05^{+0.089}_{-0.050}$	0.06	682^{+17}_{-47}
9	20	736	0.80 ± 0.080	0.08 ± 0.080	0.12	626^{+15}_{-17}
9	50	713	0.73 ± 0.073	0.15 ± 0.073	0.12	618^{+12}_{-14}
10	5	736	0.83 ± 0.083	$0.05^{+0.083}_{-0.050}$	0.12	681^{+10}_{-15}
10	20	722	0.86 ± 0.086	0.1 ± 0.086	0.04	643^{+13}_{-25}
10	50	696	0.72 ± 0.072	0.18 ± 0.072	0.10	629^{+10}_{-12}
13	5	755	0.83 ± 0.083	0.12 ± 0.083	0.05	673^{+15}_{-34}
13	20	715	0.74 ± 0.074	0.20 ± 0.074	0.06	621^{+11}_{-12}
13	50	704	0.61 ± 0.061	0.30 ± 0.061	0.09	627^{+7}_{-10}
17	5	713	0.90 ± 0.090	0.09 ± 0.090	0.01	610^{+20}_{-49}
17	20	702	0.33 ± 0.033	0.62 ± 0.033	0.05	658^{+4}_{-4}
17	50	682	0.20 ± 0.020	0.74 ± 0.020	0.06	646^{+2}_{-2}

5.2.1   Niobium-in-Solution Tests

The CCT tests discussed in the previous section were not designed with niobium dissolution in the austenite in mind. Niobium-in-solution tests were designed to investigate the effect of niobium dissolution on the transformation of the austenite. However, D_γ achieved by the grain refining step, 40μm, was much larger than the 10 and 17 μm average austenite grain diameters in the conventional CCT tests. Further grain refinement would have required strains exceeding the limits of the simulation equipment. Consequently, it was not possible to compare the results of the two sets of tests in terms of niobium dissolution exclusively; the influence of D_γ was also present.

The effect of cooling rate on transformation temperatures was pronounced for both the deformed and undeformed cases. Increasing the cooling rate from 5°C/s to 50°C/s resulted in a decrease in T_s of 62°C for austenite deformed to $\epsilon = 0.3$ and 64°C for undeformed austenite. This is reflected in the final microstructures of the test samples. There is a considerable difference between the microstructures achieved after cooling at 5°C/s and 50°C/s. See figure 5.9; 5.9a-5.9d show ferrite and bainite fractions, 5.9e and 5.9f show M/A (light phase). Whereas after 5°C/s ferrite is present in appreciable quantities, 35% for $\epsilon = 0$ and 78% for $\epsilon = 0.3$, microstructures after 50°C/s contained much reduced quantities of ferrite, 4% for $\epsilon = 0$ and 16% for $\epsilon = 0.3$. The greater fraction of ferrite in the lower cooling rate tests led to a greater fraction of M/A. In both cases, the fraction of M/A more than doubled with an increase of the cooling rate from 5°C/s to 50°C/s.

The results also show that introducing a strain of 0.3 has a significant effect on austenite decomposition. The transformation start temperature was increased rather consistently across the cooling rates: 49°C for 50°C/s, and 47°C for 5°C/s. As would be expected, there was an associated increase in the relative quantity of ferrite in the product microstructure. Interestingly, in this case the M/A fraction did not increase appreciably.

A summary of results for the Niobium-in-solution tests can be seen in
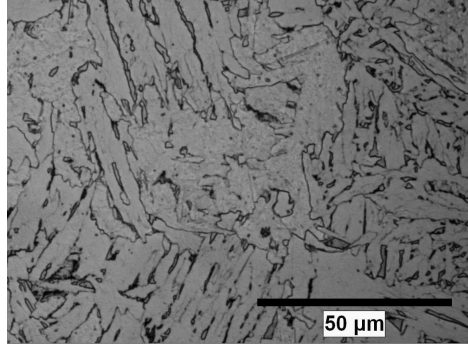
(a) $\epsilon = 0, q = 5°\mathrm{C/s}$
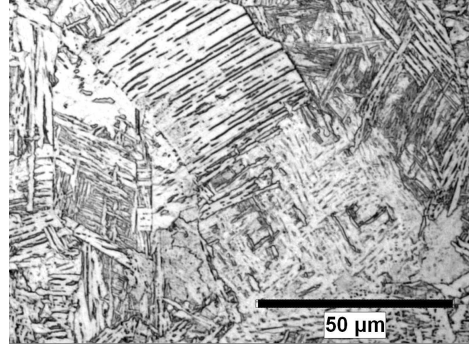
(b) $\epsilon = 0, q = 50°\mathrm{C/s}$
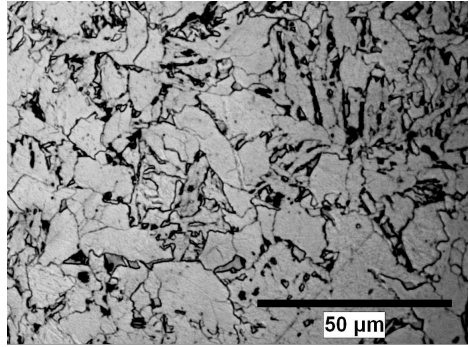
(c) $\epsilon = 0.3, q = 5°\mathrm{C/s}$
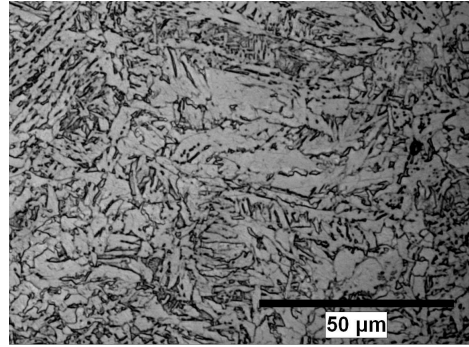
(d) $\epsilon = 0.3, q = 50°\mathrm{C/s}$
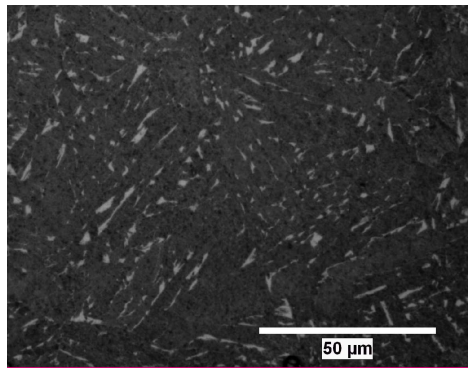
(e) $\epsilon = 0, q = 5°\mathrm{C/s}$
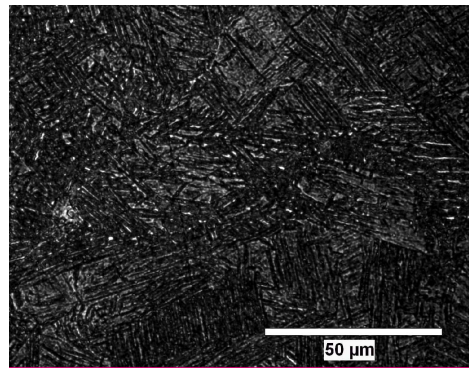
(f) $\epsilon = 0, q = 50°\mathrm{C/s}$

Figure 5.9: Nb-in-solution microstructures. (a)-(d): 2% nital etch showing ferrite, bainite; (e),(f): LePera etch showing M/A (light phase).

table 5.2.

Table 5.2: Results of quantitative image analysis, Nb in solution

D_{eff} (μm)	q (°C/s)	T_{s} (°C)	X_{f}	X_{b}	$X_{\text{M/A}}$	T_{fs}(°C)
30	5	730	0.78 ± 0.078	0.17 ± 0.078	0.05	611^{+11}_{-12}
30	20	694	0.26 ± 0.026	0.68 ± 0.078	0.06	642^{+4}_{-5}
30	50	668	0.16 ± 0.016	0.83 ± 0.078	0.01	633^{+3}_{-3}
40	5	683	0.35 ± 0.035	0.60 ± 0.078	0.05	638^{+3}_{-2}
40	20	652	0.10 ± 0.010	0.87 ± 0.078	0.03	638^{+3}_{-1}
40	50	619	0.04 ± 0.0040	0.94 ± 0.078	0.02	626^{+2}_{-2}

Effect of Initial Austenite Grain Size and Nb Dissolution

Comparing the data from the niobium-in-solution tests to the data from the conventional tests in order to evaluate the coupled effect of the much coarser D_γ and Nb in solution, it was observed that transformation proceeded at lower temperatures. For instance, T_s for undeformed austenite cooled at 50°C/s was 63°C higher for $D_\gamma = 17\mu$m than $D_\gamma = 40\mu$m. The fraction of bainite formed in the sample was thus significantly greater. As can be seen in figure 5.9 lower bainite was present in large quantities in the niobium-in-solution tests, whereas it was almost absent in the conventional CCT tests. Also, due to their more ferritic character, the fractions of M/A were greater in the conventional CCT tests.

It is not known to what extent these results can be attributed to either the greater grain size in the niobium-in-solution tests or the different states of dissolution of niobium in austenite. It is necessary to isolate these conditions by carrying out further tests where samples with $D_\gamma = 40\mu$m have niobium
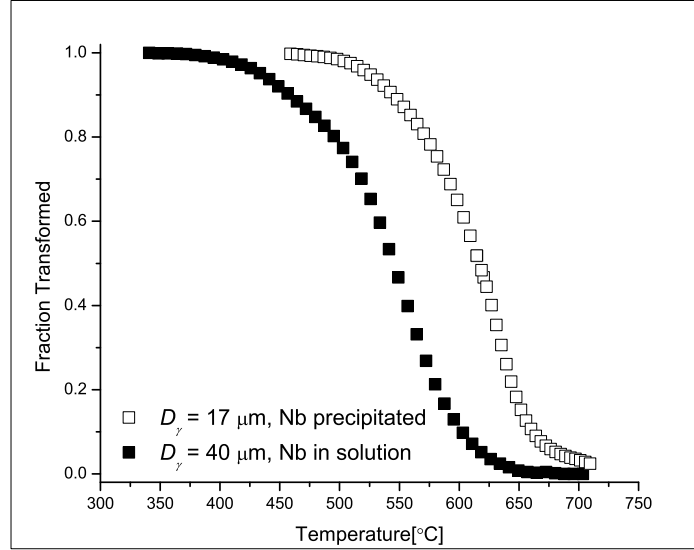
Figure 5.10: Coupled effect of D_γ and niobium dissolution on transformation in samples with $\epsilon = 0$ and $q = 50°\text{C/s}$.

precipitated in order to reliably analyse the effect of niobium dissolution on the decomposition of austenite. The precipitation of niobium in the form of carbonitrides can be achieved by precipitation treatment at $\sim 900°\text{C}$.

Chapter 6

Model

The overall transformation model consists of four individual parts. The first predicts the ferrite transformation start temperature, and the second describes the ferrite growth. The third part of the model predicts the bainite transformation start temperature and the final fraction of non-bainitic ferrite, which are assumed to be coincident. The final part describes bainite growth. The order in which the constituents of the model are presented in this chapter does not reflect their order of application in the model.

6.1   Ferrite Transformation Start

The ferrite transformation start temperature is predicted using the approach of Militzer et al [18], previously mentioned in the literature review. Assuming that carbon diffusion is rate controlling, for a spherical nucleus, the steady state growth rate is given by:

$$\frac{\mathrm{d}R_f}{\mathrm{d}t} = D_c \frac{x_c^i - x_c^\circ}{x_c^i - x_c^\alpha} \frac{1}{R_f} \tag{6.1}$$

R_f is the radius of the ferrite particle, D_c is the diffusion coefficient of carbon in austenite, x_c° is the average carbon bulk concentration, x_c^α is the equilibrium carbon concentration in ferrite, and x_c^i is the interfacial concentration of carbon, affected by manganese segregation. Integrating for a constant cooling rate q, where T_N is the temperature of nucleation,

$$R_f = \sqrt{\frac{2}{q} \int_T^{T_N} D_c \frac{x_c^i - x_c^\circ}{x_c^i - x_c^\alpha} \, dT} \tag{6.2}$$

Where r is the radius of the carbon diffusion field, the carbon concentration profile around the growing ferrite grain is given by

$$x_c(r) = \left(x_c^i - x_c^\circ\right) \left(\frac{R_f}{r}\right) + x_c^\circ \tag{6.3}$$

The temperature corresponding to 5% ferrite transformation, defined as the cessation of nucleation (site saturation), is considered as the transformation start temperature. Nucleation sites are steadily occupied, and increasing carbon concentration of austenite near nuclei due to the ejection of carbon from ferrite lowers the local driving force. These complex processes are simplified by introducing a critical carbon concentration x_c^* above which no nucleation can occur. A critical radius r^* corresponding to x_c^* can be defined:

$$r^* = \frac{x_c^* - x_c^\circ}{x_c^I - x_c^\alpha} R_f \tag{6.4}$$

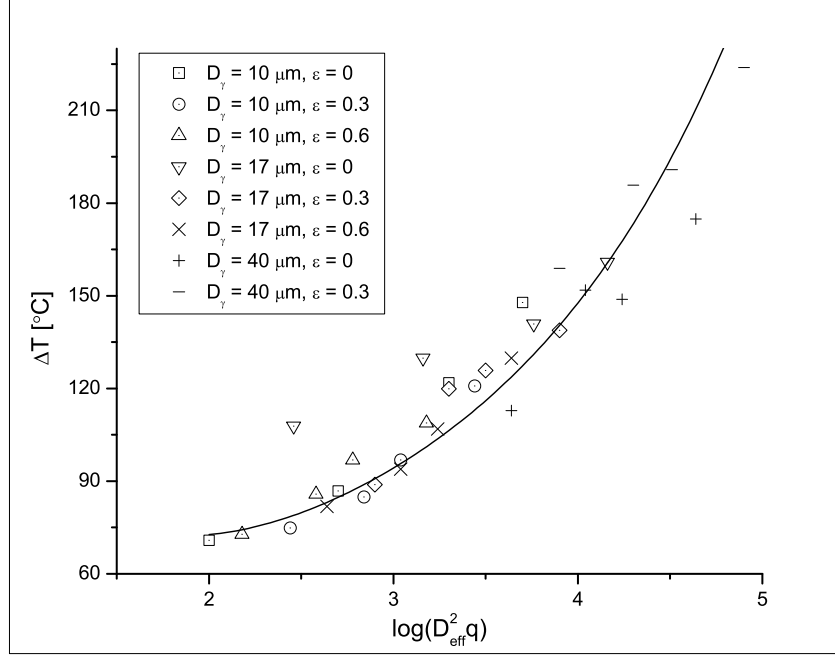Then, the transformation temperature T_S can be determined from:

Figure 6.1: Undercooling ΔT vs. $\log\left(D_{\text{eff}}^2 q\right)$

$$x_c^* - x_c^\circ = \frac{\sqrt{2M_P}\left(x_c^* - x_c^\circ\right)}{q^{1/2}D_\gamma}\sqrt{\int_{T_S}^{T_N} D_c \frac{x_c^i - x_c^\circ}{x_c^i - x_c^\alpha}\, dT} \qquad (6.5)$$

where x_c^* and T_N are used as fit parameters, and $M_P \simeq 2$ is the number of nuclei per austenite grain and D_γ is the austenite grain diameter. When $M_P r^{*2} = D_\gamma^2$, further nucleation is impossible.

Figure 6.1 shows the experimentally measured undercooling required for transformation start, along with the model predictions. The effective austenite size D_{eff} concept was used to combine the effects of initial austenite grain size and strain. Despite some scatter, single values of $x_c^* = 2.4x_c^\circ$ and $T_N = 1050K$ seem to sufficiently predict transformation start in most

64

cases.

6.2 Bainite Transformation Start

Assuming that bainite nucleation and Widmanstätten ferrite are similar, the method of Ali and Bhadeshia [37] can be used to predict the bainite start temperature [36, 10, 12]. Ali and Bhadeshia proposed that the nucleation of Widmanstätten ferrite is similar to that of martensite; that is, the activation energy for nucleation varies directly with the magnitude of the chemical driving force, the difference being that Widmanstätten ferrite nucleates under para-equilibrium conditions where carbon diffuses in contrast to the diffusion-less nucleation of martensite. They found that the critical free energy required to obtain a detectable degree of transformation is a linear function of temperature, and independent of chemical composition for low alloy steels. It is therefore possible to predict the onset of Widmanstätten ferrite nucleation by comparing the chemical driving force for the FCC-BCC transformation with critical free energy of nucleation; where the chemical driving force exceeds the critical free energy, Widmanstätten ferrite nucleation has begun.

Applying this approach to the onset of bainite formation requires quantifying the dependence of the critical free energy for bainite transformation start on temperature. The necessary data is extracted from experiments.

As discussed in the previous section, the final fraction of ferrite in each experimental sample was measured using quantitative image analysis. Assuming that ferrite formed exclusively prior to all other microstructural constituents, the measured final fraction of ferrite X_f can be used to extract the temperature at which ferrite formation ceased, from the associated transformation curve constructed from dilation data. This is a simple matter of finding the temperature on the X vs. T curve (figure 6.2) that corresponds to the value of X_f. Bainite is assumed to form immediately after ferrite. The
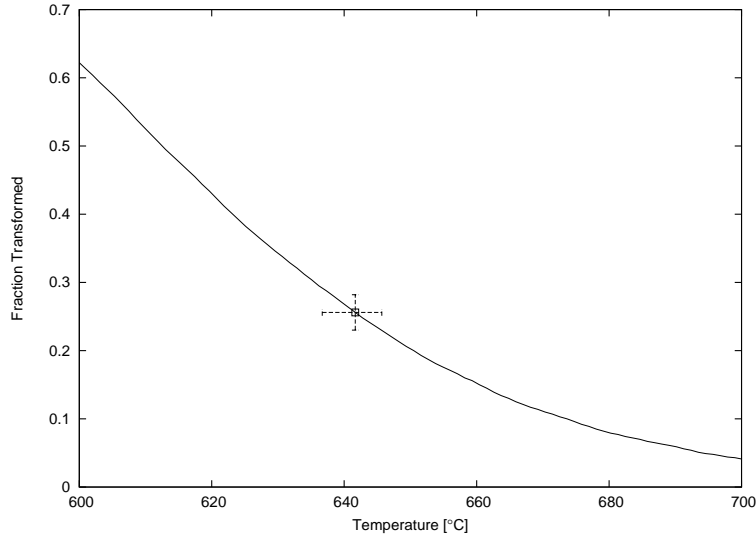
Figure 6.2: Obtaining T_{fs} from transformation curve using X_f, measured through image analysis.

temperature corresponding to X_f can then be equated with the temperature of bainite formation start, T_{bs}.

Assuming also that all carbon atoms are ejected from ferrite into the remaining austenite during transformation, the concentration of carbon in the austenite x_c^γ at the point where ferrite formation ceased can be calculated from X_f and the bulk carbon concentration x°:

$$x_c^\gamma = \frac{1}{1 - X_f} \tag{6.6}$$

Knowing T and x_c^γ allows the calculation of the chemical free energy for transformation, ΔG, using phase equilibria generated by ThermoCalc software. A set of values for the critical free energy for bainite start ΔG_{bs}^* is thus generated. Plotting ΔG_{bs}^* versus T_{bs} (figure 6.3), the linear relationship is immediately apparent, and is given by:

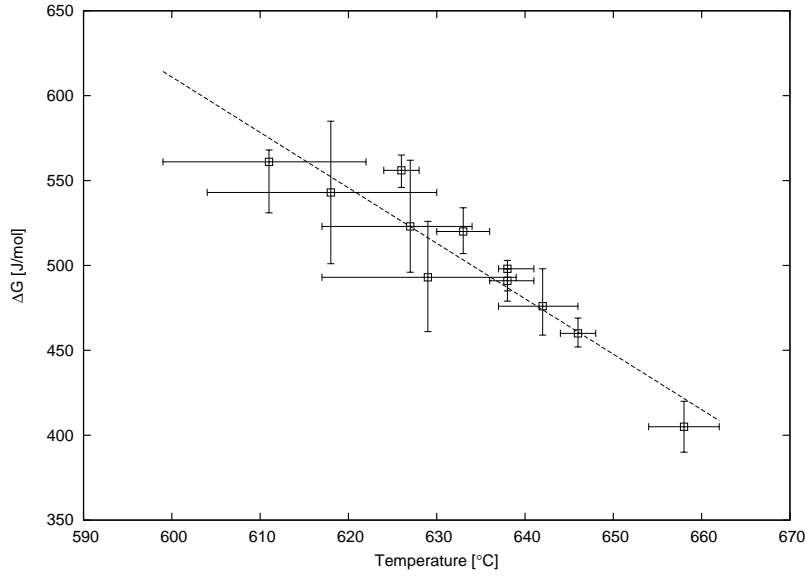$$\Delta G_{bs}^* = 2570 - 3.27 T_{bs} \tag{6.7}$$

Figure 6.3: Relationship between critical driving force for bainite formation $\Delta G_{\mathrm{bs}}^{*}$ and the temperature of bainite formation start T_{bs}

Refer to figure 6.4. The critical driving force for bainite start $\Delta G_{\mathrm{bs}}^{*}$ evaluated in this study (solid line) is compared to literature data (dotted and dashed lines) [37, 36, 10, 12]. The dashed lines indicate data for CP, DP, and TRIP steels. The close proximity of the lines seems to indicate independence from chemical composition, at least for the low alloy steels studied.

The model divides the transformation path into individual time-steps. At each time-step, the temperature and concentration of carbon in austenite (calculated from the fraction of austenite remaining, as predicted by the ferrite model discussed in the next section) are used to calculate the chemical driving force for the FCC-BCC transformation ΔG. A ΔG versus T curve can then be constructed for the transformation path. This is shown as the solid line in figure 6.5. The dotted line in figure 6.5 represents the temperature dependence of $\Delta G_{\mathrm{bs}}^{*}$ given by equation 6.7. Where ΔG is greater $\Delta G_{\mathrm{bs}}^{*}$, ferrite formation has ended, and bainite formation has begun. The intersection of the two curves is taken as T_{bs}.
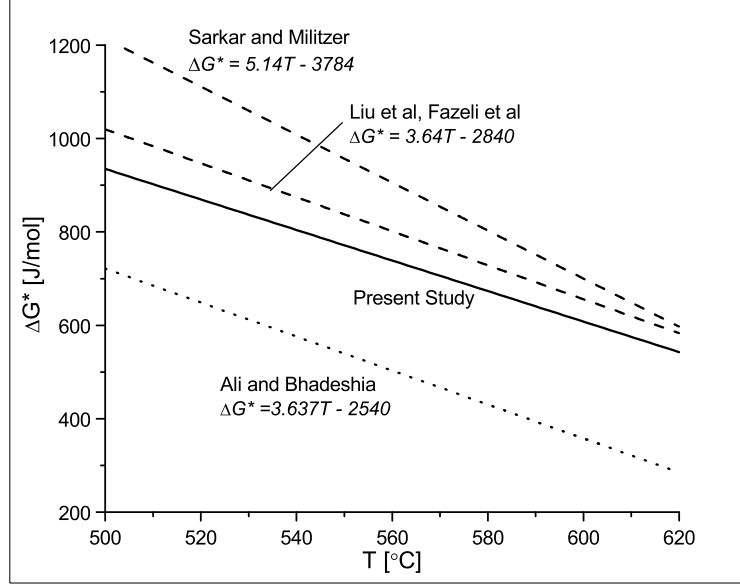
Figure 6.4: Comparison of critical driving force for bainite formation with those used in other studies.

The performance of the model can be seen in figure 6.6. Experimentally measured values of X_f are plotted on the abscissa, and model predicted values of X_f are plotted on the ordinate. The solid line represents a slope of unity and perfect agreement between experiment and model. For two of the transformation paths, the model values do not agree with experimentally measured values. This can be associated with the aforementioned image analysis measurement errors.
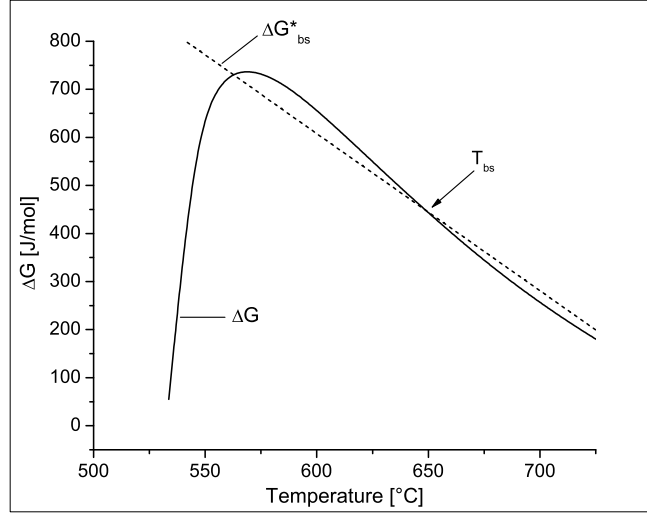
Figure 6.5: Calculating T_{bs} for the case of $D_\gamma = 10\mu\mathrm{m}$, $\epsilon = 0.6$, $q = 20$.
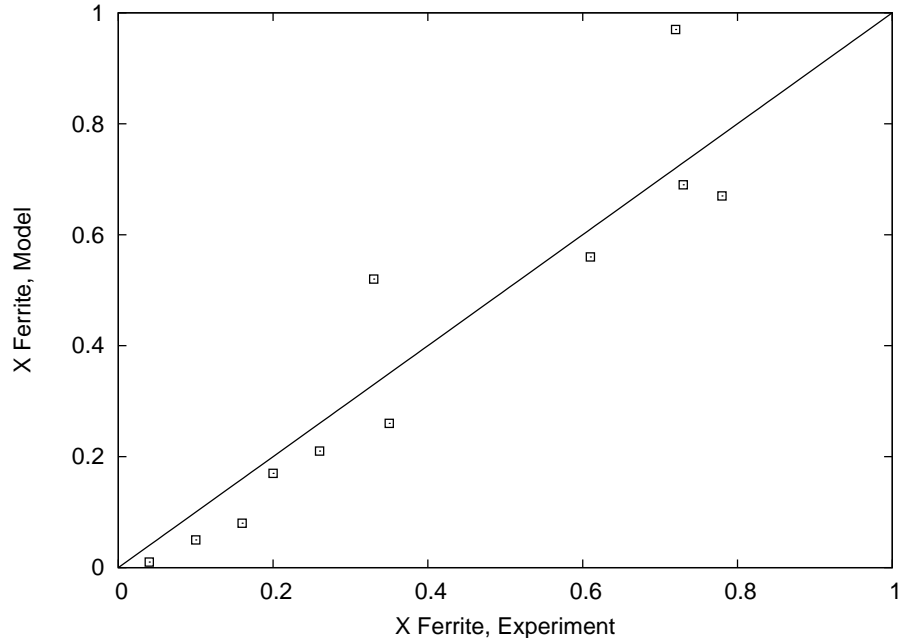

Figure 6.6: Performance of bainite start model

6.3 Ferrite and Bainite Growth

Considering an isothermal reaction at some temperature T where the time required to obtain a certain fraction transformed X is known to be $\tau(X,T)$, it is possible, using the additivity rule, to find the time required to obtain X under a constant cooling rate $q = (dT/dt)$. In this case, equation 3.4 can be used to arrive at [34]:

$$\tau(X,T) = \left(\frac{\partial T}{\partial q}\right)_X \tag{6.8}$$

Applying 6.8 to the JMAK equation, it is possible to express X as a function of q and T.

$$X(\tau,T) = 1 - \exp\left[b(T)\tau^{n(T)}\right] \rightarrow X(q,T) = 1 - \exp\left[b(T)\left(\frac{\partial T}{\partial q}\right)_X^{n(T)}\right] \tag{6.9}$$

The parameters $b(T)$ and $n(T)$ are written here as a function of temperature due to the fact that nucleation and growth are often temperature dependent.

Rios [34] devised a method to extract the isothermal data required to apply equation 6.9 from experimental continuous cooling transformation data. Where nucleation site saturation is present, the dependence of growth rate on temperature can be readily obtained from continuous cooling data. A special CCT diagram is constructed from experimental data for the transformation of concern. As opposed to the conventional method of mapping data on the $T - t$ plane, it is more convenient that the data be plotted as T vs. q. An example constructed from experimental data is shown in figure 6.7.

Each solid contour line in figure 6.7 represents a single fraction transformed. Rearranging equation 6.9, and taking the logarithm of both sides provides a useful relation:
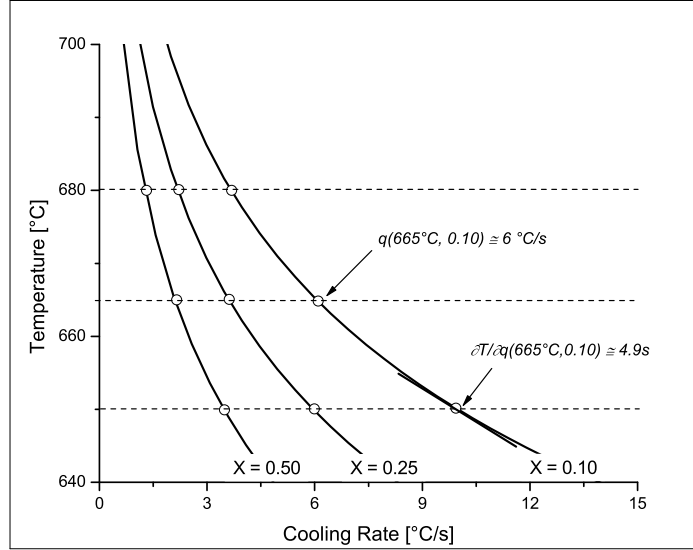
Figure 6.7: Schematic CCT diagram, plotted as T versus q.

$$\ln \ln \left(\frac{1}{1-X} \right) = \ln b(T) + n(T) \ln \left[\left(\frac{\partial T}{\partial q} \right)_X \right] \qquad (6.10)$$

In equation 6.10, fixing T results in a linear relationship whose slope is given by $n(T)$. For cases where n is independent of temperature and therefore constant, the reaction is isokinetic, and equation 6.10 can be written as:

$$\ln \ln \left(\frac{1}{1-X} \right) = \ln \left[b(T) \left(|q(X_0,T)| \left(\frac{\partial T}{\partial q} \right)_{X_0} \right)^n \right] - n \ln \left(|q(X,T)| \right)$$
$$(6.11)$$

where X_0 is some fixed volume fraction.

The value of n at some T can therefore be determined by plotting $\ln \ln \left(\frac{1}{1-X} \right)$ against $\ln q(X,T)$ for that T. Doing so, however, requires knowledge of corresponding values of X and q. This information is extracted from the con-
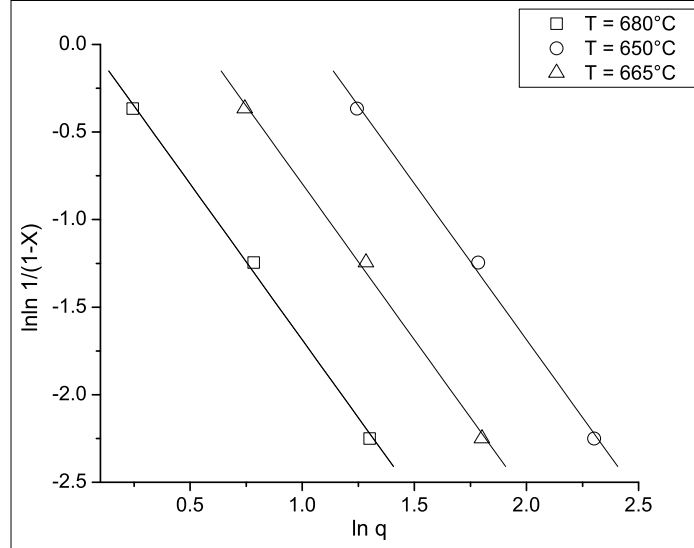
Figure 6.8: Construction to determine n for continuous cooling transformation in figure 6.7

tinuous cooling transformation diagram in figure 6.7. Intersections with the iso-X contour lines and horizontal lines (indicated in the figure with hollow circles) drawn at several temperatures within the range for which data is required, in this case 680°C, 665°C and 650°C, give values of q which would yield the fractions transformed represented by the contour lines at those temperatures. Figure 6.8 shows plots of $\ln \ln \left(\frac{1}{1-X} \right)$ versus $\ln q(X, T)$ for 680°C, 665°C and 650°C. For this temperature range, $n \simeq 1.78$ and is constant. This is an indication that the reaction is effectively isokinetic - n does not vary with temperature.

If n is known, $b(T)$ can be calculated by setting $X = X_0$ in equation 6.11. Rearranging gives

$$b(T) = \frac{\ln\left(\frac{1}{1-X_0}\right)}{\left(\frac{\partial T}{\partial q}\right)_{X_0}^n} \tag{6.12}$$

Values of $\partial T/\partial q$ are extracted from the CCT data in a manner similar to that by which q was obtained above. The value of $\partial T/\partial q$ for $T = 650°C$ and $X = 0.10$ is indicated in figure 6.7. Calculated values of $b(T)$ for a narrow range of ferrite transformation, in the case of $D_\gamma = 10\mu m$, $\epsilon = 0$, and $q = 5°C/s$, are plotted in figure 6.9. In the figure, for the above range of temperatures in this particular reaction, b is an exclusive function of T to a very good approximation. For this case, the differential form of the JMAK equation can be written as:

$$\left(\frac{dX}{dt}\right) = b(T)^{\frac{1}{n}} \cdot \left[n(1-X)[\ln(1-X)]^{\frac{n-1}{n}}\right] \tag{6.13}$$

It is quite possible however, that dX/dt is not an exclusive function of T, as is assumed by the Rios method. Conceivably, the rate of decomposition of austenite can in some cases be affected by the fraction transformed. Lusk and Jou [101] showed that the rule of additivity remains valid in cases where the rate of transformation is affected by both T and X, provided that it is a separable function of T and X. That is,

$$\frac{dX}{dt} = H(T)L(X) \tag{6.14}$$

Jia et al [35] suggested a modification of the Rios method, where b would be considered as a separable function of T and X. In essence:

$$b = f(T)g(X) \tag{6.15}$$

The differentiated form of the JMAK equation would then become:
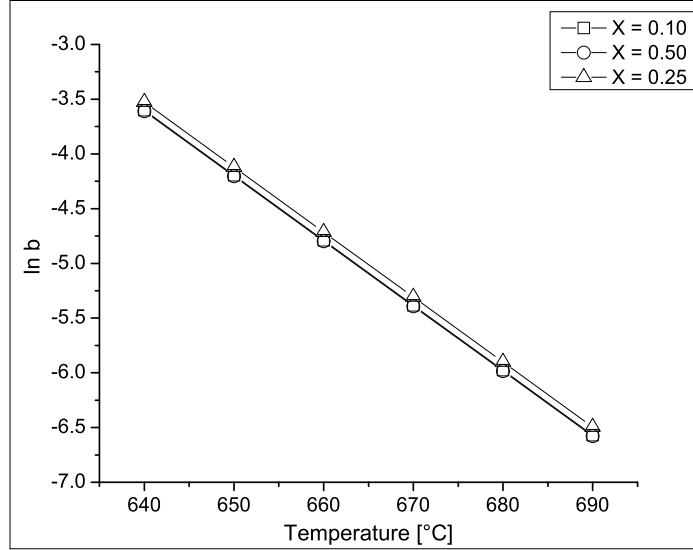
Figure 6.9: Calculated values of b versus T for the continuous cooling transformation in figure 6.7, where b is an exclusive function of T

$$\frac{dX}{dt} = \frac{b(X,T)^{\frac{1}{n}} \cdot \left\{ n(1-X)[-\ln(1-X)]^{\frac{n-1}{n}} \right\}}{1 + (1-X)\left(\frac{\partial b}{\partial X}\right)\left[\frac{\ln(1-X)}{b}\right]} \tag{6.16}$$

where

$$\frac{\partial b}{\partial X} = f(T)\frac{dg}{dX} = b \cdot \left[\frac{\left(\frac{dg}{dX}\right)}{g(X)}\right] \tag{6.17}$$

Taking the logarithm of equation 6.15, and substituting into equation 6.16 yields:

$$\ln\ln\left(\frac{1}{1-X}\right) = F(T) + G(X) + \ln\left[q\left(X_0,T\right)\left(\frac{\partial T}{\partial q}\right)_{X_0}\right]^n - n\ln\left[q(X,T)\right] \tag{6.18}$$

74

Figure 6.10: Calculated values of b versus T, where b is a function of both T and X
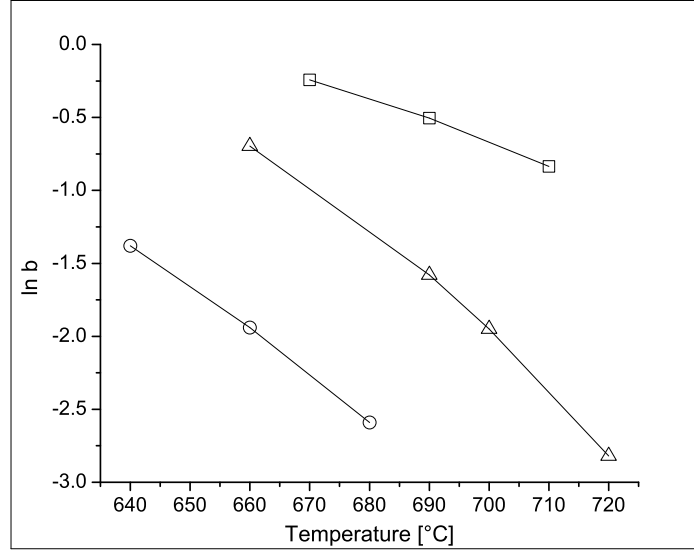
The parameters n and b (in the form of $\ln b(T,X) = F(T) + G(X)$) can be determined by following the methodology of the Rios, should n not vary with T. Rather, they must be obtained numerically. Figure 6.10 shows a plot of $b(T,X)$ versus T for a reaction in which b is strongly dependent on X. This was the case for the majority of experimental data in this study, for both ferrite and bainite.

Implementation of Modified Rios Method

Transformation data sets acquired from experiments during the present study are divided into ferritic and bainitic sections. Austenite decomposition is assumed to begin with the formation of ferrite, and transition to bainite at later stages of transformation. The fraction transformed for each of the two constituents is normalized by a different method. For ferrite formation,

75

the experimental fraction of austenite transformed X_{exp} at each recorded temperature datum is divided by the para-equilibrium ferrite fraction X_{PE} at that temperature, such that the normalized fraction of ferrite X_α is given by:

$$X_\alpha = \frac{X_{\mathrm{exp}}}{X_{\mathrm{PE}}} \tag{6.19}$$

The normalized bainite fraction transformed X_b, on the other hand, is defined as

$$X_b = \frac{X_{\mathrm{exp}} - X_f}{1 - X_f} \tag{6.20}$$

where X_f is the previously defined final fraction of ferrite. CCT diagrams were constructed and n was extracted following the Rios method. It was found that n values for both the ferritic and bainitic portions of the transformation curve showed some temperature dependence, suggesting that additivity might not be fulfilled. This result was not surprising for the bainitic case, where sympathetic nucleation of ferrite plates invalidates the assumption of site-saturation, and the shifting morphologies and mechanisms affect growth rates. For the ferrite case, the temperature dependence of n might be explained by referring to the microstructural morphology of the product. Figure 6.11 shows an extreme example of the temperature dependence of n encountered during analysis. The range of constituents defined for this model as 'ferrite' is quite broad, encompassing morphologies from polygonal ferrite to acicular ferrite and structures at the transition point to bainite. It was found, however, that selecting an average value of n for each one of the ferritic and bainitic reactions yielded satisfactory predictions.

The rate parameter b is extracted from the data as previously discussed. As expected, b shows a significant dependence on the fraction transformed, especially for cases where little polygonal ferrite is present. The modified form of the Rios treatment is therefore implemented. An equation that in-
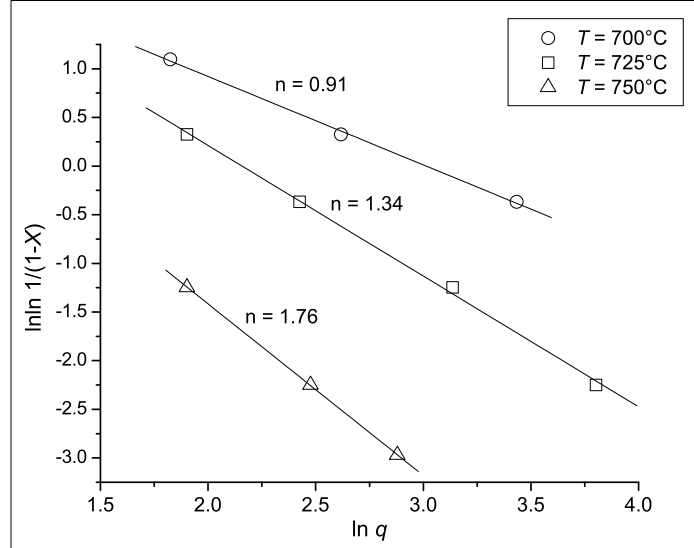
Figure 6.11: Temperature dependence of n. Data shown is for $D_\gamma = 10\mu$m, $\epsilon = 0.6$.

cludes the effect of both T and X is used to fit the calculated b values, where:

$$\ln b = a(T - T_0)^2 + c\ln(1 - X) + d \qquad (6.21)$$

The fit parameters T_0 and c have been found to be independent of the initial conditions of the austenite. Single values of T_0 and c are established for each of the ferritic and bainitic transformations. Parameters a and d on the other hand show strong dependence on the initial austenite conditions. To account for this in the ferritic portion of the transformation, the effective austenite grain size D_{eff}, defined previously, is added to equation 6.21, such that:

Table 6.1: Ferrite and bainite growth model parameters

Parameter	Ferrite	Bainite
n	1	0.5
a_1	-1.41×10^{-4}	9.3×10^{-6}
a_2	1.56×10^{-4}	1.62×10^{-6}
T_0	602	884
c	0.1	0.35
d_1	-0.05	-0.11
d_2	0.52	0.01

$$\ln b = [a_1 \ln D_{\text{eff}} + a_2] \cdot (T - T_0)^2 + c \ln(1 - X) + d_1 D_{\text{eff}} + d_2 \qquad (6.22)$$

In the bainite model, D_{eff} is replaced by D_{rem}, or the effective average diameter of remaining austenite, assuming spherical geometry. This is done to account for the reduced size of the austenite after ferrite formation has proceeded, assuming ferrite grows on the austenite grain boundaries towards the centre of spherical austenite grains. D_{rem} is defined as

$$D_{\text{rem}} = D_{\text{eff}} (1 - X_f)^{\frac{1}{3}} \qquad (6.23)$$

Values for n and the parameters describing b are listed in table 6.1. A value of $n \simeq 1$ for the ferrite portion of transformation is consistent with results from other studies [7, 10, 12, 35]. This value suggests the presence of site-saturation and one-dimensional growth of ferrite from austenite grain boundaries [19]. The bainitic transformation $n \simeq 0.5$ is slightly lower than values reported in literature [12, 35] for low alloy steels.

Figure 6.12 shows some calculated transformation fractions compared to experimental data for the ferrite portion of the reaction. Examples of predic-
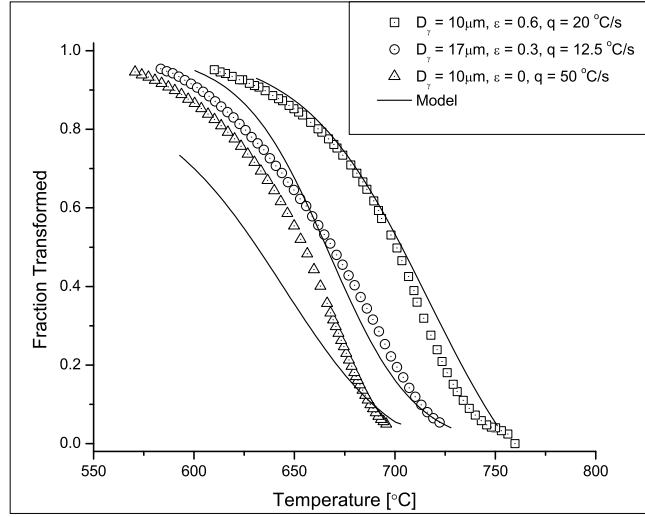
Figure 6.12: Experimental data, prediction of ferrite start and growth models.

tions by the bainite growth model are shown in figure 6.13. Generally good agreement is achieved for most data sets. The use of the JMAK equation and additivity principle seems to offer an adequate prediction of the transformation kinetics. Not all predictions are good, however; the ferrite prediction for the case of $D_\gamma = 10\mu m/\epsilon = 0/q = 50°C$, shown in figure 6.12, is such an example. An effort is made to formulate fit parameters that would help avoid discrepancies between calculated and experimental values for industrially relevant cases. In the more relevant cases where deformation is present, the model provides good agreement with experiments.

Improvement of the model fit requires a more in-depth study of the effects of the initial austenite condition (D_γ,ϵ) and fraction transformed on the rate parameter b. The form of equation 6.22 is empirical. A more theoretical approach could yield better results. Furthermore, the effects of niobium in solution and niobium carbonitride precipitates on b were not considered in
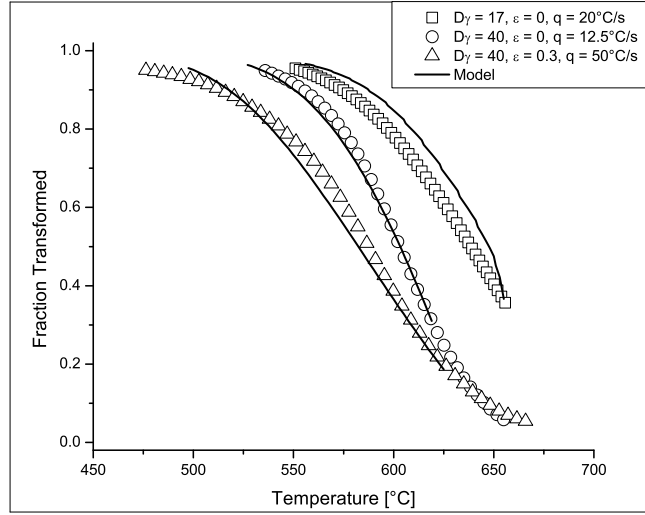
Figure 6.13: Experimental data, and predictions of bainite growth model.

the present model. A study of literature suggests significant influence of the state of niobium on transformation behaviour. The solute drag effect of niobium on the advancing interphase, serves to slow growth, while fine niobium carbonitride precipitates serve as extra nucleation sites.

It is expected that as the initial austenite grain size is increased beyond those studied in this investigation, increased sympathetic nucleation during bainite formation will effect the quality of the model predictions. However, these grain sizes are not of major concern, as its not expected that they will be encountered during hot-rolling.

Chapter 7

Conclusions

Experiments were conducted on a Ferrite-Bainite steel to investigate its transformation behaviour under varying processing conditions including reheat temperature, degree of strain, and cooling rate. To this end, data has been acquired for austenite grain growth, softening following deformation in the austenite, and the kinetics and proportions of ferrite and bainite in the steel. Based on the data, the effect of varying the initial austenite conditions (austenite grain size and retained strain), and cooling rate on the transformation behaviour of the steel have been reported and analysed.

Existing techniques for predicting the transformation start temperature, ferrite growth, bainite formation start temperature, and bainite growth have been used to model the decomposition of austenite. The model can be used to predict the temperature and kinetics of transformation, and the final fractions of ferrite and bainite in the steel.

As study of the effect of the state of niobium dissolution in the austenite during transformation on transformation behaviour has been initiated. Further tests in this area are required in order to make any meaningful conclusions.

7.1 Future Work Recommendations

The following are recommended as improvements to the model, and extension of the experiments:

- The fit function describing the JMAK equation rate parameter b in the ferrite and bainite models could be improved. Although the current form seems to provide a satisfactory fit for industrially relevant conditions, it does not perform ideally for all cases. Further study of the effect of initial austenite grain size and retained strain on b is recommended.

- Reducing the rather large measurement error for the final fraction of ferrite would significantly improve its predictive capabilities. An EBSD technique utilizing misorientation gradients has been investigated by Zaefferer et al [102] as a method to determine the fraction of bainite; an attempt could be made to implement this technique to supplement image analysis to this end.

- Further study of the effect of the state niobium dissolution in austenite on transformation behaviour is necessary for any meaningful analysis of the subject, or its implementation in the model. CCT tests could be devised that follow the same procedures for austenitization, niobium dissolution and austenite grain refinement as the niobium-in-solution tests, with the modification that samples are held above the Ae_3 temperature for enough time to ensure full precipitation of niobium carbonitrides. In this way data can be generated for cases where niobium is precipitated, but where the initial austenite grain size is identical to the 40μm in the niobium-in-solution samples. This will make it possible to investigate the effect of the state of niobium dissolution in isolation.

Bibliography

[1] A. DeArdo, Int. Mater. Rev. 48 (2003) 371 – 402.
URL `http://www.ingentaconnect.com/content/maney/imr/2003/00000048/00000006/art00002`

[2] A. Le Bon, J. Rofes-Vernis, C. Rossard, Met. Sci. 9 (1975) 36 – 40.

[3] C. Sellars, J. Whitemean, Metal Sci. 13 (1978) 187 – 194.

[4] T. Senuma, M. Suehiro, H. Yada, ISIJ Int. 32 (3) (1992) 423 – 432.

[5] M. Suehiro, T. Senuma, H. Yada, K. Sato, ISIJ Int. 32 (3) (1992) 433 – 439.

[6] J. Beynon, C. Sellars, ISIJ Int. 32 (1992) 359 – 367.

[7] D. Liu, F. Fazeli, M. Militzer, ISIJ Int. 47 (12) (2007) 1789 – 1798.

[8] D. Liu, M. Militzer, W. Poole, Mater. Sci. Forum 539-543 (2007) 4391–4396.

[9] F. Fazeli, Phd thesis, Ph.D. thesis, UBC (2005).

[10] D. Liu, F. Fazeli, M. Militzer, W. Poole, Metall. Mater. Trans. A 38 A (4) (2007) 894 – 909.

[11] F. Fazeli, M. Militzer, Steel Res. 76 (2005) 815 – 821.

[12] S. Sarkar, M. Militzer, Mater. Sci. Tech. 25 (9) (2009) 1134 – 1146.

[13] W. F. Smith, Structure and Properties of Engineering Alloys, 2nd Edition, McGraw-Hill, 1993.

[14] J.-C. Zhao, M. R. Notis, Mater. Sci. Eng. 15 (4-5) (1995) 135 – 208.

[15] H. Okamoto, J. Phase Equilibria 13 (1992) 543.

[16] D. A. Porter, K. E. Easterling, Phase Transformations in Metals and Alloys, 2nd Edition, CRC Press, Taylor and Francis Group., 1992.

[17] H. Bhadeshia, J. Christian, Metall. Trans. A 21 A (4) (1990) 767 – 797.

[18] M. Militzer, R. Pandi, E. Hawbolt, Metall. Mater. Trans. A 27 A (6) (1996) 1547 – 1556.

[19] M. Militzer, E. Hawbolt, T. Meadowcroft, Metall Mater Trans A 31 A (4) (2000) 1247 – 1259.

BIBLIOGRAPHY

[20] M. Avrami, J. Chem. Phys. 7 (12) (1939) 1103–1112.

[21] M. Avrami, J. Chem. Phys. 8 (2) (1940) 212–224.

[22] M. Avrami, J. Chem. Phys. 9 (2) (1941) 177–184.

[23] W. Johnson, R. Mehl, AIME trans. 135 (1939) 416 – 442.

[24] A. Kolmogorov, Bull. Acad. Sci. USSR. Ser. Math. 3 (1937) 355359.

[25] M. Umemoto, N. Komatsubara, I. Tamura, J. Heat Treating 1 (1980) 57 – 64.

[26] H. Han, S.-H. Park, Mater. Sci. Tech 17 (2001) 721 – 726.

[27] T. I. et al, Thermomechanical Processing of High-strength Low-alloy Steels, Buttersworths, 1988.

[28] E. Scheil, Eisenhuettenwesen 8 (1934-35) 565 – 567.

[29] J. Cahn, Acta Metall. 4 (6) (1956) 572 – 575.

[30] J. Cahn, Acta Metall. 4 (5) (1956) 449 – 459.

[31] P. Campbell, E. Hawbolt, J. Brimacombe, Metall. Trans. A 22 A (11) (1991) 2779 – 2790.

[32] R. Kamat, E. Hawbolt, L. Brown, J. Brimacombe, Metall. Trans. A 23 A (1992) 2469 – 2690.

[33] S. Malinov, Z. Guo, W. Sha, A. Wilson, Metall Mater. Trans A 32 A (2001) 879 – 887.

[34] P. Rios, Acta Materialia 53 (18) (2005) 4893 – 4901.

[35] T. Jia, M. Militzer, Z. Liu, in Press.

[36] F. Fazeli, M. Militzer, in: J. Howe, E. Laughlin, J. Lee, D. Srolovitz, U. Dahmen (Eds.), Solid-Solid Phase Transformaitons in Inorganic Materials 2005, TMS, Warrendale PA, 2005, p. 835.

[37] A. Ali, H. K. D. H. Bhadeshia, Mater. Sci. Tech. 6 (1990) 781 – 784.

[38] M. Enomoto, H. Aaronson, Metall. Trans. A 17 A (8) (1986) 1381 – 1384.

[39] P. Clemm, J. Fisher, Acta Metall. 3 (1955) 70 – 73.

[40] W. Lange, M. Enomoto, H. Aaronson, Metall Trans. A 19 A (1988) 427 – 439.

[41] M. Enomoto, H. Aaronson, Metall Trans A 17 A (8) (1986) 1385 – 1397.

[42] M. Enomoto, W. Lange III, H. Aaronson, Metall. Trans. A 17 A (8) (1986) 1399 – 1407.

[43] S. Offerman, N. van Dijk, J. Sietsma, S. Grigull, E. Lauridsen, L. Marguiles, H. Poulsen, M. T. Rekvelt, S. van der Zwaag, Science 298 (2002) 1003 – 1005.

[44] C. Hutchinson, A. Fuchsmann, Y. Brechet, Metall Mater. Trans. A 35 A (2004) 1211 – 1221.

BIBLIOGRAPHY

[45] C. Zener, J. App. Phys. 20 (1949) 950 – 953.

[46] J. Bradley, H. Aaronson, Metall. Trans. A 12 A (10) (1981) 1729 – 1741.

[47] M. Hillert, J. Agren, Scripta Mater. 50 (2004) 697 – 699.

[48] H. Aaronson, W. Reynolds Jr., G. Shiflet, G. Spanos, Metall. Trans. A 21 A (6) (1990) 1343 – 1380.

[49] H. K. D. H. Bhadeshia, Bainite in Steel, 2nd Edition, IOM Communications, 2001.

[50] T. Tanaka, H. Aaronson, M. Enomoto, Metall. Mater. Trans A 26 A (1995) 535 – 545.

[51] T. Tanaka, H. Aaronson, M. Enomoto, Metall Mater. Trans A 26 A (1995) 547 – 559.

[52] T. Tanaka, H. Aaronson, M. Enomoto, Metall Mater. Trans A 26 A (1995) 561 – 580.

[53] D. Quidort, Y. Brechet, Acta Mater. 49 (2001) 4161 – 4170.

[54] H. Aaronson, M. Hall, Metall. Mater. Trans. A 25 A (9) (1994) 1797 – 1819.

[55] H. Bhadeshia, D. Edmonds, Metall. Trans. A 10 A (7) (1979) 895 – 907.

[56] M. Hillert, A. Borgenstam, J. Agren, Scripta Mater. 62 (2010) 75 – 77.

[57] G. Spanos, H. Fang, H. Aaronson, Metall. Trans. A 21 A (6) (1990) 1381 – 1390.

[58] P. Shipway, H. Bhadeshia, Mat. Sci. Eng. A A201 (1-2) (1995) 143 – 149.

[59] H. Bhadeshia, D. Edmonds, Acta Metall. 28 (9) (1980) 1265 – 1273.

[60] G. Rees, H. Bhadeshia, Mater. Sci. Tech. 8 (11) (1992) 994 – 996.

[61] T. Nakamura, S. Nagakura, in: S. Int. Conf. on Martensitic Transformations - ICO-MAT '86, JIM, 1986, p. 386.

[62] Y. Ohmori, T. Maki, Mater. Trans. JIM 32 (8) (1991) 631 – 641.

[63] M. Kang, J. Sun, Q. Yang, Metall. Trans. A 21 A (4) (1990) 853 – 858.

[64] S. Matas, R. Hehemann, AIME Trans. 221 (1) (1961) 179 – 185.

[65] G. Rees, H. Bhadeshia, Mater. Sci. Tech. 8 (11) (1992) 985 – 993.

[66] H. K. D. H. Bhadeshia, Metal Sci. 16 (1982) 159 – 165.

[67] W. Reynolds Jr., H. Aaronson, G. Spanos, Mater. Trans. JIM 32 (8) (1991) 737 – 746.

[68] M. Enomoto, Metall. Trans. A 25 A (1994) 1947–1955.

[69] R. Heheman, K. Kinsman, Metall Trans A 3 A (1972) 1077.

[70] H. Aaronson, G. Spanos, W. Reynolds Jr., Scripta Mater. 47 (3) (2002) 139 – 144.

[71] J. Rigsbee, H. Aaronson, Acta Metall 27 (1979) 351.

BIBLIOGRAPHY

[72] M. Hillert, Metall. Mater. Trans. A 25 A (9) (1994) 1957–1966.

[73] B. Muddle, J. Nie, G. Hugo, Metall. Mater. Trans. A 25 A (9) (1994) 1841 – 1856.

[74] H. Aaronson, B. Muddle, J. Nie, Scripta Mater. 41 (2) (1999) 203 – 206.

[75] M. Hillert, Scripta Mater. 47 (2002) 175 – 180.

[76] A. Borgenstam, M. Hillert, J. Agren, Acta Mater. 57 (2009) 3242 – 3252.

[77] C. Atkinson, Proc. R. Soc. Lond. A 378 (1981) 351 – 368.

[78] M. Hillert, Jernkont. Ann. 141 (1957) 757 – 764.

[79] G. Horvay, J. W. Cahn, Acta Metall. 9 (1961) 695 – 705.

[80] G. Ivantsov, Dokl Nauk SSSR 58 (1947) 567 – 569.

[81] R. Trivedi, Metall Trans. 1 A (1970) 921 – 927.

[82] C. Zener, Trans. AIME 167 (1946) 550 – 583.

[83] T. Minote, S. Torizuka, A. Ogawa, M. Niikura, ISIJ Int. 36 (1996) 201 – 207.

[84] E. Palmiere, C. Garcia, A. DeArdo, Metall Mater Trans A 27 A (1996) 951 – 960.

[85] S. Hansen, J. Vander Sande, M. Cohen, Metall Trans A 11 A (1980) 387 – 402.

[86] J. Speer, S. Hansen, Metall Trans A 20 A (1989) 25 – 38.

[87] M. Luton, R. Dorvel, R. Petkovic, Metall Trans A 11 A (1980) 411 – 20.

[88] M. White, W. Owen, Metall Trans A 11 A (1980) 597 – 604.

[89] L. Cuddy, Metall Trans. A 12 A (1981) 1313–20.

[90] C. Fossaert, G. Rees, T. Maurickx, H. Bhadeshia, Metall Mater. Trans A 26 A (1995) 21–30.

[91] G. Rees, J. Perdrix, T. Maurickx, H. Bhadeshia, Mater. Sci. Eng. A 194 (1995) 179–186.

[92] I. Timokina, E. Pereloma, P. Hodgson, Mater. Sci. Tech. 17 (2001) 135–140.

[93] J.-C. Cao, Q.-Y. Liu, Q.-L. Yong, X.-J. Sun, J. Iron Steel Res. Int. 14-3 (2007) 51–55.

[94] M. Suehiro, Z.-K. Liu, J. Agren, Acta Mater. 44 (1996) 4241–4251.

[95] C. Klinkenberg, K. Hulka, W. Bleck, Steel Res. Int. 75 (2004) 744 – 752.

[96] J. Brechet, C. Hutchinson, H. Zurob, C. Sinclair, Steel Res. Int. 78 (2007) 210 – 215.

[97] J. Park, Y. Lee, Scripta Mater. 56 (2007) 225–228.

[98] F. Humphreys, M. Hatherly, Recrystallization and Related Annealing Phenomena, 2nd Edition, Pergamon, 2004.

BIBLIOGRAPHY

[99] S. Lacroix, Y. Brechet, V. M., D. Quidort, K. M., T. Iung, in: E. Damm, M. Merwin (Eds.), Austenite Formation and Decomposition, TMS, Warrendale PA, 2003, pp. 367 – 379.

[100] A. Cota, D. Santos, Mater Char. 44 (2000) 291 – 299.

[101] M. Lusk, H. Jou, Metall. Mater. Trans. A 28 A (2) (1997) 287 – 291.

[102] S. Zaefferer, P. Romano, F. Friedel, Journal of Microscopy 230 (2008) 499–508.